UNIVERSITÀ DEGLI STUDI DI PADOVA

Facoltà di Scienze Matematiche, Fisiche e Naturali

Dipartimento di Fisica e Astronomia "Galileo Galilei"

TESI DI LAUREA MAGISTRALE IN FISICA

LOWER LIMIT ON DARK MATTER LIFETIME IN PERSEUS GALAXY CLUSTER

LAUREANDA:
Camilla Maggio

SUPERVISOR:
Prof. M.Mariotti
CO-SUPERVISORS:
Dott. M.Doro
J.Palacio

ANNO ACCADEMICO 2014/2015

Contents

1 INTRODUCTION

The world we can see everyday is not all of what exist in Nature. The "normal" matter, i.e. the baryonic matter, of which the trees, the houses, the earth, the animals, us, all what is around are composed, takes part only to the 4% of the total amount of things present in the Universe. This little amount of matter, that seems to us to be filling all the Universe, shares the cake with two other, not fully understood, components: Dark Matter (23%) and Dark Energy (73%), at least as far as we know. In fact, despite our knowledge on these percentages, we do not know so much about the real composition of non-baryonic matter and many efforts have been done and will be done to study it. The main information that we have about these two components of the Universe are that the former is something like a mass filling the space and at most interacting very weakly with the Standard Model particles, while the latter is related to the expansion of the Universe and has been introduced as a constant in the equation of the general relativity formulated by Albert Einstein.
In particular, the aim of this thesis is to improve our knowledge on DM, looking at its decay in the galaxy cluster Perseus. What we would like to reach with this search is an observation of the DM decay, and maybe to win the Nobel prize, but what we expect really is to find lower limits on the lifetime of DM particles stronger than the ones just observed. To calculate these limits, the observations of the MAGIC telescopes and new analysis methods have been used and will be described here.
The main body of the thesis is structured in five chapters, excluding this introduction. At the beginning one can find a general description on DM: the evidences that led to guess for its presence at different scales, a few possible candidates taken from the breaking of ad hoc symmetries introduced in the Standard Model (not built to fulfill DM particle properties!), the few knowledge we have of DM and a list of various experiments to study DM and its properties, taking advantage of the different kind of interactions that it has with the Standard Model particles, together with some results obtained. The third chapter will be based on the description of MAGIC, the two telescopes used for the observation of the source of interest, taking into consideration the main characteristics of them. The thesis will continue with a brief introduction on the galaxy clusters, in particular on Perseus, in an astronomical point of view and describing the features concerning DM and its decay. Chapter 5, together with chapter 6, are the most interesting chapters of this work because they describe all the analysis done, beginning from the data reconstruction and finishing with the presentation of the results obtained. As conclusion, a comparison with the results obtained by other experiments and what we will do in the future is reported.

2 DARK MATTER

2.1 Evidences

In 1933 F. Zwicky, a Swiss astronomer, compared the mass measurement of Coma cluster using luminous and gravitational estimations. Assuming the system is virialized[1], the rotational velocity of an object gravitationally bound to the system, as a function of the distance r from the center, is

$$v = \sqrt{\frac{GM(r)}{r}}$$

where G is the Newton's constant and $M(r)$ is the distribution of mass contained in a sphere of radius r. If one considers $M(r)$ as constituted only by baryons, it obtains an $M(r)$ increasing with the volume inside the galactic disk and $M(r) \sim 0$ outside, expecting a rotational curve like the dashed one in the plot of Fig.1. However, Zwiky found a discrepancy between the calculus of the mass from the velocity dispersion of galaxies in the cluster and the photometric measures. Consequently to this fact, he reached the conclusion that the resulting curve could not be due only to the visible matter, but also to a missing type of it that generates a gravitational field without emitting light. Thus the name "dark matter". Moreover, from the photometric measures he found that the luminous mass was only 1/400 of the virial mass used to fit the observed velocities.

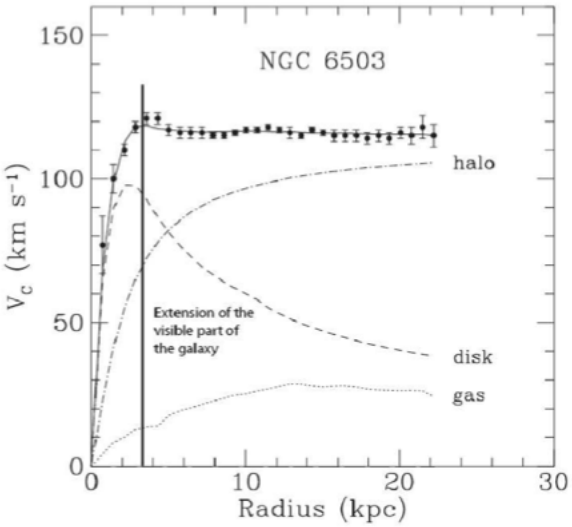

Figure 1: Rotational curves for the spiral galaxy NGC 6503. Credits:[18].

[1]The gravitational interacting particles system is stable, i.e. its potential energy is twice the relative kinetic energy $U = -2K$.

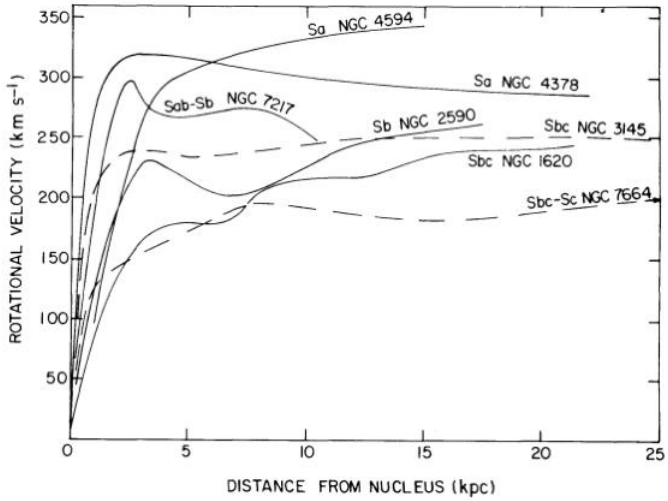

Figure 2: Rotational curves of different galaxies. Credits: [31].

For many years physicists and astronomers could not believe on the experimental observations interpreted through this non luminous missing matter, until the 70's, when a series of experiments make them to reconsider their point of view. In that years the American astronomer V. Rubin convinced the scientific community measuring the rotational velocities of objects gravitationally bounded to galaxies. She observed that these gas, stars, etc. were not following the Kepler's rotation law around the visible center of the galaxy and that their velocities did not decrease outside the galactic disk, were the mass density would have been $\simeq 0$. Afterwards, different research groups pointed their attention to the DM distribution in a galaxy or in a cluster and they found that it is approximately spherical and that it stays in correlation 5 at 1 with the baryonic matter [23], showing a density that decreases from the center to the border of this DM halo. The halo should be a static sphere, not rotating, that comes from the gravitational collapse of the initial inhomogeneities of the Universe and that envelops the baryonic matter composing the galaxy. Thus, taking in consideration this large amount of DM in comparison to visible matter, one can explain the variations on the rotational velocities. A few example of these are present in the plot of Fig.2.

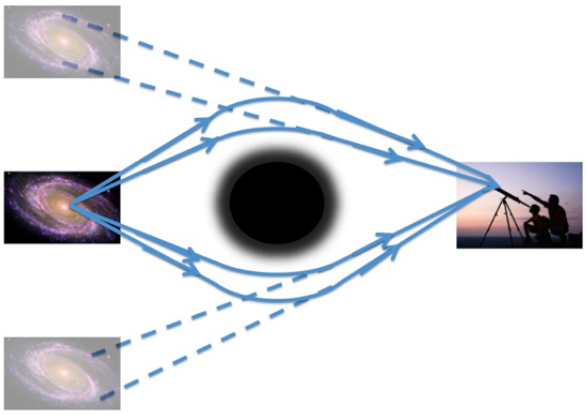

Figure 3: Gravitational lensing technique. Credits: [22].

Another strong evidence, at larger scales, of this new form of matter concerns the gravitational lensing. This is a technique based on Einstein's theory of gravitation, in which it is postulated that light-rays move into geodesic[2] and it is predicted that the energy-matter density introduces local curvature in the space-time. When coming from distant sources, in fact, light-rays curve because of massive objects by the side of their ways, like galaxies or galaxy clusters (see Fig.3). In the particular case in which the source, the lens and the observer are aligned, if one looks from the Earth at the light coming, one can notice the Einstein's ring: something like a circle formed by the symmetrically reflected images of the sources and centered around the real position of it. In the last years, the results of this lensing were able to get the amount of mass causing the deflection and it has been noticed that the visible matter measured is not sufficient to create that kind of deflection, confirming rotational curves hypothesis.

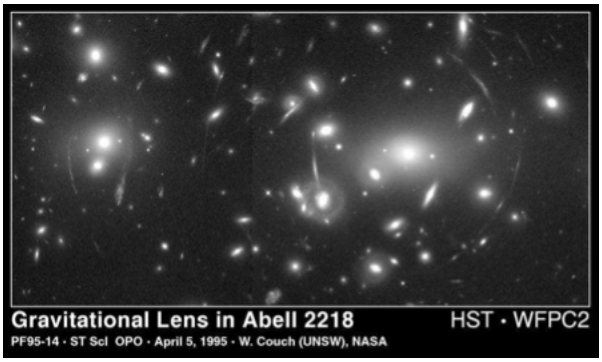

Figure 4: Effect of DM in the galaxy cluster Abell 2218. Credits: [18].

An example of this can be seen by studying the deflection angle of the Einstein's ring in the right image of Fig.4. Moreover, the improvement on gravitational lensing studies

[2]Generalization of the notion of straight line in a curved space-time.

allows to produce maps of the present-day dark matter distribution in the local Universe as a projection of it in two dimensions.

Figure 5: Picture of the Bullet Cluster 1E0675-558: the gaseous interacting part had been coloured in red, while the dark matter part in blue. Credits: [18].

At the same scales, the Bullet Cluster 1E0675-558, that consists of two colliding galaxy clusters, is considered one of the strongest evidences of the presence of dark matter. During the interaction of the two clusters of galaxies, the spatial segregation between the radio emission and the luminous emission is clearly visible (Fig.5). The X-ray image reflecting the gas component denotes distinguishing features compared to the gravitational lensing image, which bring us back the mass distribution. This fact led to assume the presence of a missing luminous matter: since DM is supposed to interact gravitationally and very weakly (on the contrary of baryonic matter that is also electromagnetically interacting, emits light and radiate energy), it can intersect almost undisturbed, while the gas is decelerated due to the viscosity.

Taking into consideration, now, the whole Universe, and, in particular, referring to the Cosmic Microwave Background (CMB), another evidence of the existence of DM is present.
CMB consists of a radiation emitted during the re-combination era, when the temperature was low enough to permit electrons to combine with atomic nuclei without interfere with the photons, that were free to propagate in the Universe with a stabilized temperature that is now 2.73 K. It is a strong prediction of the modern cosmology theory that supposes that the Universe is expanding and that, in the past, it was smaller and hotter than now. However, the fluctuations of the baryonic matter measured were

not enough to create the structures we can see everyday. Thus, the anisotropies in this CMB have lead to add DM as a component of the Universe[3].
For the first time, Planck satellite defined how much of the microwaves of the CMB received had come from the primordial Universe, how much from the extragalactic space, how much from our galaxy and how much from the instrument itself and inferred the DM component. A map of this CMB Universe can be seen in Fig.6.

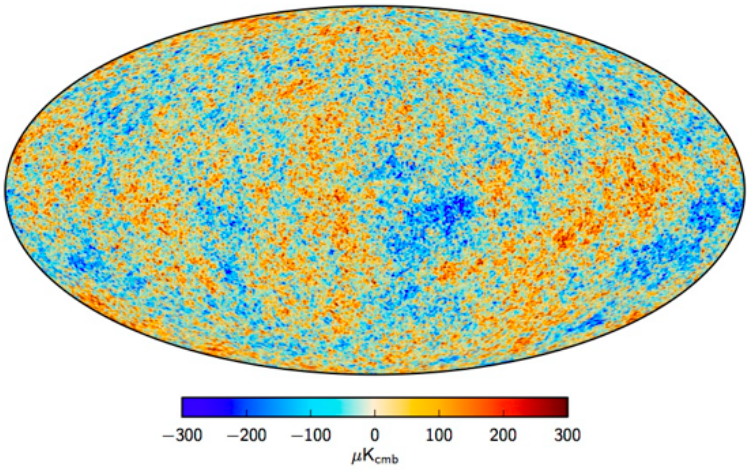

Figure 6: Thermal map of the Universe drawn by a joint baseline analysis of Planck satellite, WMAP mission and 408 MHz observations. Credits: [1].

In particular, the values of the different components are the following: $\Omega_{DM}h^2 = 0.1187 \pm 0.0017$ of DM, $\Omega_b h^2 = 0.02214 \pm 0.00024$ of baryons and $\Omega_{DE}h^2 = 0.692 \pm 0.010$ of dark energy (DE), where $h = 0.697 \pm 0.024$ is the Hubble constant[4] and $\Omega_i \equiv \rho_i/\rho_c$ is the ratio of the energy density of each component and of the critical density[5], i.e. the value of the energy density to have a spatially flat Universe. The pie chart of the components of the Universe is shown in Fig. 7.

[3]Knowing the particle density at the freeze-out, the moment in which the particles come out from equilibrium, and scaling the volume of the Universe, one cam have the estimation of relic density and of the energies end temperatures of the particles today.

[4]It is the present expansion rate of the Universe in units of 100 km/Mpc s.

[5]$\rho_c \equiv \frac{3H_0^2}{8\pi} = 1.88 \times 10^{-29} h^2$ g/cm^3

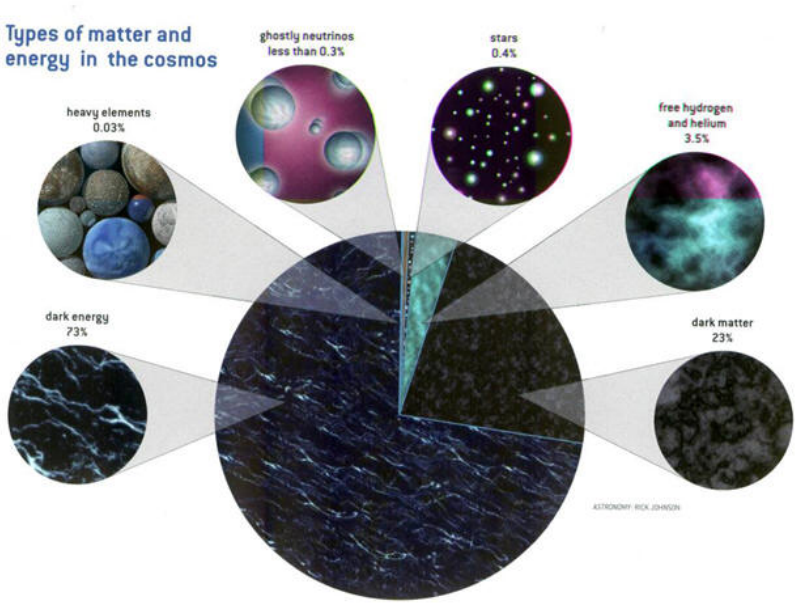

Figure 7: Pie chart of the composition of the Universe. Credits:[9].

The abundance of baryons has been obtained from four independent measurements: the relative height of the peaks in the angular power spectrum of CMB anisotropies, the abundance of light chemical elements generated in the Big Bang Nucleosynthesis (BBN), Baryon Acoustic Oscillations and absorption lines of the light of Quasars [23].

2.2 Our Knowledge on Dark Matter

What one can learn from the evidences written above is, then, that it is present this large and non luminous amount of non-luminous mass that played a role on the structure formation. A problem due to DM, then, has been introduced: one has to describe the large amount of DM in the Universe without using Standard Model particle as candidates. Looking at the issue from a cosmological point of view, it is sensible to search for a massive particle calculating its energy density in the Universe beginning from the freeze-out era. What we obtain is

$$\Omega_\chi \backsimeq \frac{10^{-27}\mathrm{cm}^3\mathrm{s}^{-1}}{<\sigma_a v>}$$

where the cross-section times velocity is averaged over the temperature and has to be exactly $10^{-27}\mathrm{cm}^3\mathrm{s}^{-1}$ for a unitary relic density, condition perfectly fulfilled by massive particles with weak interactions at hundred GeV scale, the so-called "WIMP miracle". These WIMPs (Weakly Interacting Massive Particles) can be considered, then, as one of the CDM[6] (Cold DM) candidates, because of their non-relativistic behavior at the

[6]"Cold" because of the temperature of the particles in comparison to their mass at the moment of the freeze-out.

moment of the freeze-out. The need to have a "cold particle" is due to structures formation in consequence to the density fluctuations: if the DM particles pressure due to the free-streaming velocity had not been smaller than the one associated to their mass, we would not have seen the present Universe, as the relativistic DM particles would not have permit baryonic particles to aggregate into structures. Nevertheless, the CDM is not the only type of DM theorized, as one can see in a pictorial way in Fig.8:

- hot DM (HDM): the particles were relativistic at the freeze-out (mass of the order of the eV or smaller). Candidates for this DM are the neutrinos;
- warm DM (WDM): the particles have masses around the keV and are becoming non relativistic in this era. Candidates for these are the gravitinos, the sterile neutrinos and some non-thermal WIMPs;
- cold DM (CDM): the masses of these particles are in the GeV-TeV scale and these were non relativistic at the freeze-out. The most studied candidates are the neutralinos and the Kaluza-Klein states.

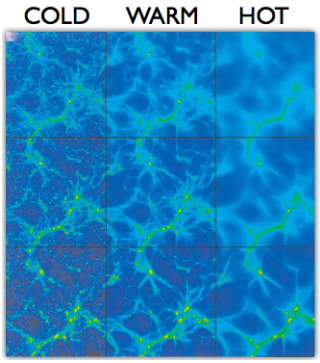

Figure 8: Particular of the substructures created by different types of DM, obtained from the N-body simulations (for more details see § 4.1) in the Milky Way. Credits: [27].

Other particles less massive than CDM are possible candidates as, for example, the axion-like particles, that have a non-thermal origin, but we will discuss it later.

2.2.1 Dark Matter Candidates

Consequently to experimental observations, then, DM particles, in addition to having the characteristics set out previously, have to be stable, or with mean life-time $\gg t_U$ (lifetime of the Universe) and do not have to interact with light. Thus, being unable to cool by radiating photons during galaxy formation, the bulk of DM must be dissipationless. No Standard Model particles, except for the neutrino, can fulfill all these requirements and so new particles, coming from the breaking of symmetries introduced ad hoc to solve some SM problems, are the best candidate until now.
Let's see a part of the zoo of candidates (Fig.9) in the following lines.

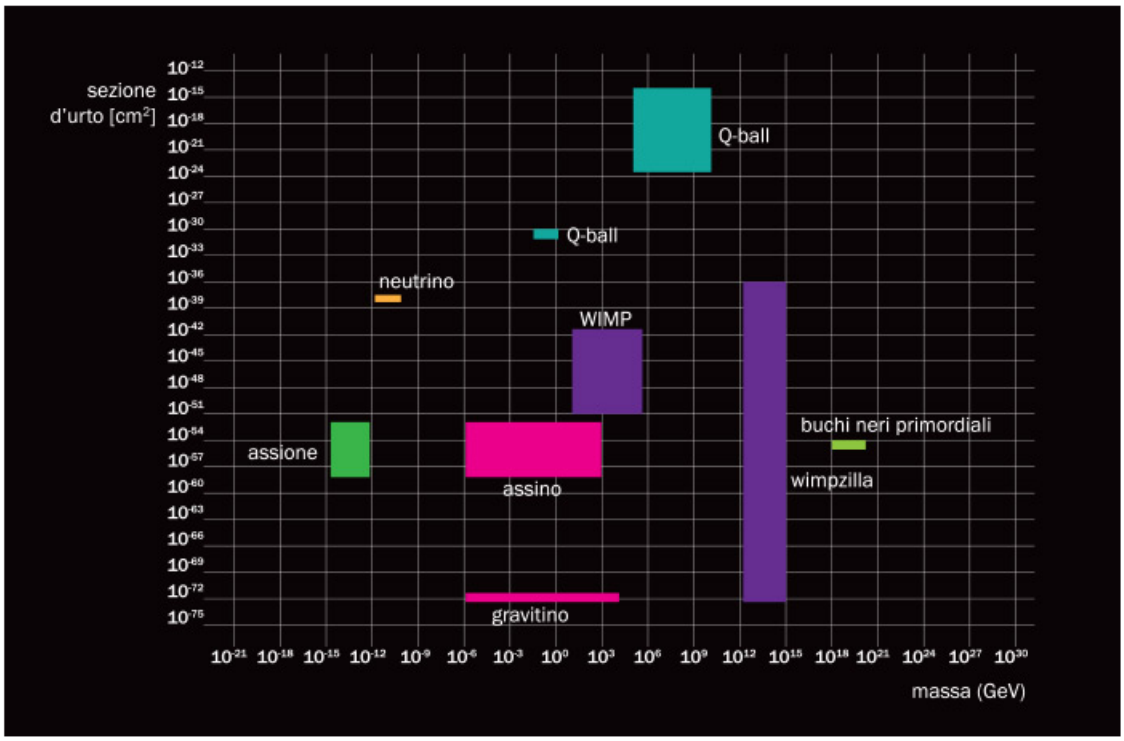

Figure 9: Schematic representation of DM candidates as a function of their mass. Credits: [10].

Beginning from the lightest particles, and going on to the heaviest, we can find:

Axion This new light pseudoscalar boson, chargless and spin-0 particle (a Goldstone boson[7]), comes out from the spontaneous breaking of the Peccei-Quinn symmetry[8]. It acquires its mass of $10^{-5} - 10^{-2}$ eV by non perturbative effects and, despite this, it is a non relativistic DM candidate. In the end, as a good DM particle has to do, the axion interact very poorly with matter and only oscillation into photons in magnetic fields or in cosmic distances could allow us to detect them.

Neutrino It is a particle that fulfills all conditions to be a good DM candidate, except for its mass and its density in the Universe. In fact, measurements done by Superkamiokande (in Japan) tell us that oscillations between neutrino's flavor are of the order of 0.05 eV and, consequently, the masses of the three

[7]Goldstone's theorem states that, for each breaking of a generator of a global symmetry G, one obtains a scalar boson at spin-0 and null mass, the Goldstone boson.

[8]Since we can not observe the violation of the CP symmetry in strong interactions, a term dipendent on θ had been adden in QCD Lagrangian.To make this one correspomding to the reality, θ has to be very small or equal to zero. In order to reach this purpose, Peccei and Quinn proposed to use a dynamic field to originate θ, instead of considering it as a constant.The breaking of the symmetry comes when the average value of this term in the vacuum is different from zero.

species of neutrinos have to be of the same order. The neutrino density is then too small to be the total amount of DM density, as the equation to find the former is

$$\Omega_\nu = \frac{\rho_\nu}{\rho_c} = \frac{\sum_i m_i n_\nu}{\rho_c} \backsimeq \frac{\sum_i m_i}{30\,\mathrm{eV}}$$

where ρ_ν and ρ_c are the neutrino desity and the critical density respectively, $\sum_i m_i$ is the sum of the mass of the neutrinos and n_v is their the number density, equal to $n_\nu = \frac{3}{11} n_\gamma^{CMB}$ with $n_\gamma^{CMB} = 410.5\,\mathrm{cm}^{-3}$. Moreover, if we had considered neutrinos as the unique kind of DM, we would not have had our present Universe, as the structures would have been formed in a later period because of the numerous interactions of the neutrinos, being relativistic particles.

Kaluza-Klein state A substitute of the SuperSymmetry, of which I will talk later, are the Unified Extra Dimensions (UED) theories, in which a 4-dim space-time is believed to be embedded in a larger frame with flat extra dimensions where all the SM fields are allowed to propagate. Into this scenario, Kaluza-Klein states for each SM particle are present and meet a symmetry (KK parity) that states that the contributions to SM arise only at loop level, in which the particles are produced in pair, and that the lightest KK particle (LKP) is stable. Then, LKP is a good DM candidate.

Wimpzilla Possible candidate of DM directly created at the end of the Inflation[9] thanks to the gravitational interaction. Its mass is of the order of 10^{13} GeV and it decays into SM particles with UHE or EHE CRs.

Other possible candidates can be added to this list, like primordial black holes, sterile neutrinos, brane DM, little higgs, mirror matter and so on, but, for this work, I will concentrate on SuperSymmetry (SUSY) and the DM candidates it gives us.
This theory pairs bosons with fermions conjecturing the existence of particles with similar quantum number and spin+1/2 for each SM particle: if the superpartner is a fermion, one adds the prefix s- to the SUSY particle, on the contrary, one adds the suffix -ino. It is important to notice that the purpose of SUSY was not to create an ad-hoc DM model, but to cope with theoretical problems of the SM: the mass hierarchy problem[10], the observation of strong CP violation in experiments and the imperfect unification of the gauge couplings at the Planck scale ($M_{Pl} \sim 10^{19}$ GeV). Among all various types of SUSY theories, the most considered is the Minimal SUSY model (MSSM), that has the minimum number of free parameters. To avoid the problem of symmetry breaking, that leads to a proton lifetime far shorter than the age of the Universe (Super-Kamiokande

[9]Theory affirming that the Universe has been subjected to a period of very rapid expansion, after the Big Bang, because of a negative pressure generated by the energy of a quantistic field called inflaton.

[10]The mass measured of the Higgs boson ($m_h \sim 125$ GeV) is too small compared to that one it would have had because of radiative corrections ($\sim 10^{16}$ GeV).

is a Japanese experiment that, among its purposes, looks also for this [25]) and that is due to the different masses between particles and super-particles, an ad-hoc symmetry, the R-parity, has been introduced.

Neutralino This MSSM particle is a superposition of fermionic spartners of SM bosons (the bino $\tilde{B}^0$, superpartner of the weak hypercharge gauge boson, the wino $\tilde{W}_3^0$, superpartner of the electroweak interaction mediating boson, and the Higgsinos $\tilde{H}_u^0$, $\tilde{H}_d^0$, superpartners of the neutral Higgs bosons) and it shows up in four states $\tilde{\chi}_{1...4}^0$. The lightest of these one (Lightest Supersymmetric Particle, LSP), that is defined as

$$\chi \equiv \tilde{\chi}_1^0 = n_{11}\tilde{B}^0 + n_{12}\tilde{W}_3^0 + n_{13}\tilde{H}_d^0 + n_{14}\tilde{H}_u^0$$

where n_{ii} are the weights of each superparticle, is the DM candidate, since it is stable, if the R-parity is a conserved symmetry, and all the heavier particles can decay into it.

Other SUSY DM candidates could be the gravitino, that is a supersymmetric field of the supergravity theory, the sneutrino and the axino.

2.3 Dark Matter Annihilation/Decay

After having had a look at a few of this DM candidates, what follows is that some of them could annihilate or, maybe, decay, e.g. in the case of the R-parity violation, giving Standard Model particles as products. This is the reason why we look for them through our searches, of which I will talk in the next paragraph. In particular, we consider here WIMPs as DM particles.
WIMPs have normally QCD (Quantum ChromoDynamics) interactions with ordinary matter and also annihilate producing SM particles. In fact, WIMPs are supposed to be Majorana particles, i.e. particles that are their own antiparticles, and for this reason they can annihilate among one another. As primary products of their annihilation we can find: quark, fermions, especially heavy states, gauge bosons, Higgs bosons, photons and internal Bremsstrahlung. This last one is a boosted emission of γ-rays that permits to restore the helicity balance in processes that would be forbidden without this emission. Several are the secondary products of the annihilation, but what is interesting here is the fact that, if we can measure γ-rays as final products of the annihilation, the cutoff of their spectrum can give us the mass of a DM particle. It is important to notice, in particular, that these gamma-rays are not only primary or secondary products of DM annihilation/decay, but are produced also through Inverse Compton (IC)[11] scattering of the less energy photons produced in the annihilation/decay.
As far as the decay of DM concerns, a description a little more in-depth of the processes involved and of the products is left for chapter 6. Nevertheless, I will introduce here

[11] Process in which an electron/positron hits a photon transferring to it energy and momentum. In this particular case, the electrons/positrons give enough energy to the photons to permit them to have at least the energy of the order of the MeV.

some basic concepts to understand what leads us to the search of this decaying DM and which is the reason why we look for it through VHE γ-rays. Two are the general point of view when one takes in consideration the DM decay: either DM is stable in consequence to the imposition of ad hoc extra symmetries in the theoretical model, or it is unstable, but very long-lived. Assuming that the DM is decaying, its decay rate per unit kinetic energy T and unit volume can be written as

$$Q(T, \vec{r}) = \frac{\rho_{DM}(\vec{r})}{m_{DM}} \sum_f \Gamma_f \frac{dN^f}{dT}$$

where ρ_{DM} and m_{DM} are the density at the position $\vec{r}$ and the mass of a DM particle respectively, $\vec{r}$ is the point of the decay, Γ_f is the partial decay rate in the channel f and $\frac{dN^f}{dT}$ is the energy spectrum of the particles produced in that channel. Among the final states f we can find anti-matter, neutrinos, photons (VHE γ-rays among them) and other SM particles. Until now, no evidence for decaying DM has been found and only lower limits on its lifetime could be set. The more recent one excludes lifetimes shorter than 10^{28} s for mass between a few hundred GeV and ~ 1 TeV [8], a value surely longer than the age of the Universe that is .

2.4 Dark Matter Searches

Looking at what affirmed by theories, proposed theoretical models and experimental observations, hoping that DM would not be secluded in the Dark Sector (region that does not have any interaction with the SM particles) the experimental apparatuses have to cope with very massive particles, that interact very weakly and that do not decay or have a lifetime longer than that of the Universe. Moreover, one has to consider that DM tends to aggregate gravitationally into substructures, mostly in the center of galaxies or in clusters, and that, in particular, its density in the solar system is around $\rho \approx 0.3$ GeV/cm^3. Having in mind all these remarks and the fact that DM particles can interact directly or indirectly with SM particles, three complementary ways of detections can be used, as you can see in the plot of Fig.10.

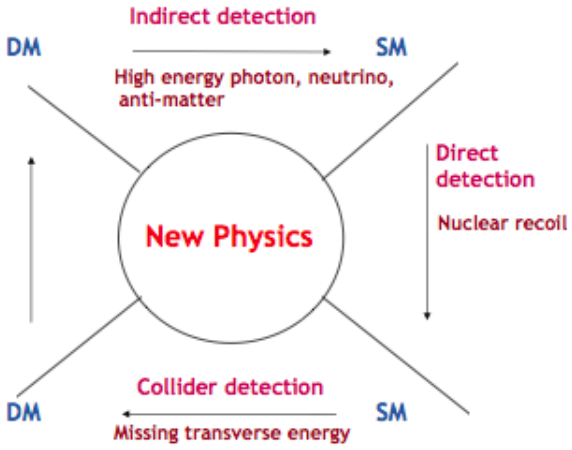

Figure 10: Schematic plot of the different directions of DM experiments. Credits: [11].

- **Direct Detection**

  Even if DM is so weakly interacting, when passing through dense targets it can be observed indirectly looking at the products of nuclear recoil. In non-relativistic limits, this scattering can be divided into two classes: the spin-independent (SI) one that couples to the mass of the detector nuclei, increasing the scattering rate as $\sigma \propto A^2$, where A is the mass number, and the spin-dependent (SD) one that couples to the spin of the nuclei. Since a possible detection rate is $1 - 10^5$recoil $\mathrm{kg}^{-1}\mathrm{week}^{-1}$with cross section of the order of 10^{-43} cm^2, an important issue for this kind of experiments is to reduce the background and keep it under control. Several are the sources of the background, such as: CRs, gamma photons and electrons due to the decay of radioactive isotopes present in the rocks and in the air around the detectors and the electronic recoils induced by the detector apparatus. To decrease this huge amount of background, the detectors are located in underground laboratories, are provided by shields of lead and reinforced concrete together to a system of veto to distinguish between electronic recoil events and nuclear recoil signals, use high purity materials and create Monte Carlo statistical simulations to simulate the background.

  Nowadays, more than 20 direct detection experiments are running or are under construction and they can be divided into different classes: heat and ionization detectors, that require crystal semiconductor material and cryogenic cooling and reveal both charge signal from ionization after nuclear recoil and heat signal (CDMS, CoGeNT, CRESST, EDELWEISS, TEXONO, CDEX); scintillation detectors, that measure the light of scintillation coming from the passage of DM (DAMA, KIMS); noble liquid experiments (XENON, ZEPLIN, PandaX); superheated liquid experiments (COUPP, PICASSO, SIMPLE); etc.

  The output of such experiments is the number of interactions measured, but, because of this is compatible with the background, only a limit in the rate of

recoil per kg of detector can be set. This last one gives us limits in the DM particle (WIMP)-nucleon interaction cross section, after having studied it with proper theoretical models. However, results like those of DAMA and CoGeNT seem to be inconsistent with those coming from higher sensitivity experiment such as XENON and CDMS and this is today an open question that, maybe, can be solved upgrading the detectors to larger volumes, improving the sensitivity for DM-nucleon scattering cross section.

- **Collider Detection**

  This kind of experiments are based on missing transverse energy (MET) technique. Since the DM mass is supposed to be $\lesssim O(10^2)$ GeV in some theoretical models, DM particles can be obtained at the high energy colliders LHC, Tevatron and, probably, at the planned ILC. After having been produced, the particles escape the detector bringing with them their energy, that will miss from the total amount because of their extremely weak interactions. The MET, quoted previously, can be obtained by associated jets, photons or leptons, looking at the momentum conservation in the plane perpendicular to the beam pipe, while the total missing energy can be reconstructed only in $e^+ - e^-$ colliders (in hadron colliders the exact energies of initial partons are unkown). Moreover, in hadron colliders, this process is affected by the background reactions that produce neutrinos and single top and by false positives. Nevertheless, there is not a unique manner to produce these DM particles: one way is to obtain them in pair directly from collisions of SM particles and to detect them through an additional energetic jet or photon (mono-jet or mono-photon), from the initial state radiation, used as trigger signal (ATLAS); the other way is to produce DM particles as cascade decay elements of some heavier new particles, following the SUSY model (CMSSM[12]).

  Thus, accelerator experiments lead to define constraints on DM particle masses, but with the upgrade of LHC at 14 TeV center of mass energy there are great expectations for new discoveries.

- **Indirect Detection**

  The annihilation or decay products of DM, that are SM particles, are what such experiments look for, as these signals (γ-rays, neutrinos, positrons, antiprotons, antideuterons and synchrotron radiation) can be detected from them. Since these particles could be confused with the CRs background particles, appropriate systems to distinguish them had been created. They consist in satellite or balloon-borne experiments (located outside the atmosphere to avoid its shield that stops all light wavelenghts except those from UV to IR and the radio waves, as you can see in Fig.11), that observe directly DM products interacting inside the detectors, and ground-based telescopes, that profit by secondary products of interaction of γ-rays in the atmosphere.

[12]Constrained Minimal SuperSymmetric Model [11].

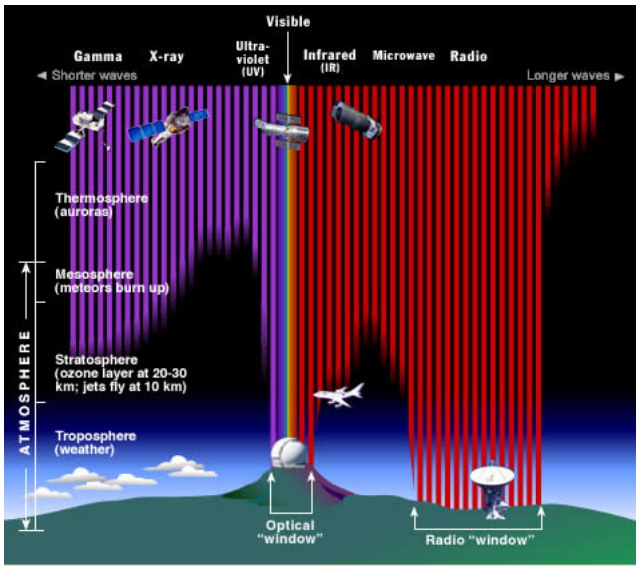

Figure 11: Spectrum of the EM radiation penetrating in Earth's atmosphere.Credits: [28].

Of fundamental importance here is the fact that the charged particles, produced in annihilation/decay of DM particles, are deflected when propagating in the interstellar space, as it is filled with magnetic fields, and consequently the source of information will get lost. Then, the only possibility to extract infos from such particles is to go back indirectly to the energy spectra. On the contrary, γ-rays and neutrinos travel undisturbed through the Universe allowing to trace back to the source where we point our instruments, expecting a high DM density.

One part of the photons detectable is that one coming directly from DM annihilation/decay and it is the hardest to be observed. In fact, to couple directly with photons, DM particles, being neutral, need a loop Feynman diagram in which DM first annihilates into two virtual charged particles and then these last ones annihilate into two real photons. Once observed them, the result is a monoenergetic spectrum giving us approximately the mass (half of it for decaying DM) of DM particles, as they move non-relativistically today, and that it is seen like the "smoking gun" of DM signal, since no astrophysical source can produce that spectrum. The other part of photons, easier to detect given the larger flux, come from the cascade decays into γ-rays of quarks, bosons, etc. that have been produced in DM annihilation/decay. They give us a continuum spectrum whose drawback is that it doesn't have distinctive features from the astrophysical background γ-rays.

In the last years, experiments have been focused on various subject in relation to their characteristics and their capability to detect particles at different energy ranges. The γ-ray probe in the range between about $\sim$ 100 MeV and several 100 GeV has been made by pair-conversion telescopes on satellites, foremost the

Fermi Large Area Telescope (LAT), the most sensitive γ-rays detector in space. Above 100 GeV one can reach better sensitivities using Imaging Air Cherenkov Telescopes (IACT), such as HESS, MAGIC (see chapter 3) and VERITAS. Making a comparison between the two kinds of experiments, we can see that IACTs' effective areas are of the order of 10000 m^2, as they utilize the Earth's atmosphere (for more details see chapter 5), while satellites effective areas are more or less of a square meter. However, the latters have a larger field of view (FoV) than IACTs (2.4 sr for Fermi-LAT in comparison to $\sim$ 5 deg of IACTs) and a more efficient background suppression. Keeping an eye on the results obtained, a new one, based on PASS8[13] event selection, has been presented in Fermi symposium in 2014 . Fermi-LAT excluded generic WIMPs (in the b-channel) up to masses of 100 GeV but, despite its improved sensitivity, it did not confirm the DM interpretation of the above mentioned GC excess. On the other side, most stringent constraints could be obtained by IACTs around 1 TeV. In Fig. 12 are presented the results for b-quark channels of the different experiments and what we can reach with new ones.

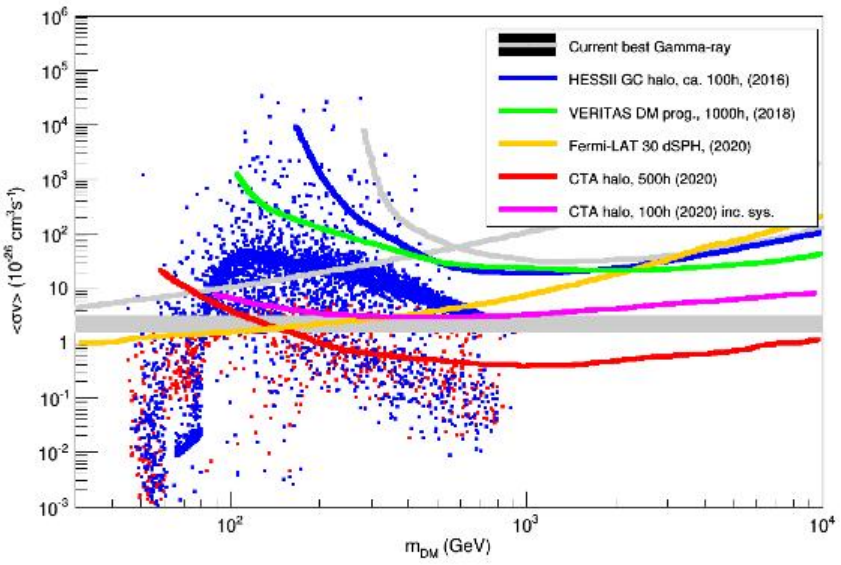

Figure 12: Current most relevant constraints and future simulations on annihilation cross-section as a function of the mass for quark-channels. Credits: [16].

As one can see, CTA (Cherenkov Telescope Array) is one of the new projects that will improve the measurement sensitivity and will focus its attention to the energy range between 100 GeV and 100 TeV, as it is predicted to probe the thermal WIMP cross-section among these masses. The experiment is composed

[13]Fermi-LAT event-level analysis.

of an array of about 80 telescopes with a sensitivity of a factor 10 better than the previous ones and an energy range from about 10 GeV to 40 TeV. Also pair conversion telescopes, having all deep calorimeters with a resolution of the order of 1%, are planned: GAMMA-400, DAMPE (DArk Matter Particle Explorer) and HERD (High Energy cosmic Radiation Detector).

As far as the charged cosmic ray probe concerns, other kind of experimental setups are used. The excess of anti-protons and positrons had been detected mainly by PAMELA experiment, ATIC and, more recently, by AMS-02 (Alpha Magnetic Spectrometer that operates on the International Space Station since 2011), as one can see a in a recent version of the plots in Fig.13-14 (ATIC is not present because it is older). PAMELA is a spectrometer mounted on a Russian satellite launched in 2006. It has a geometric factor (GF)[14] of about 20 cm^2sr, differently from AMS-02 that has a GF larger by 1 to 2 decades. The positron excess detected by this experiment, and confirmed by AMS-02, suggests to add WIMPs annihilation as source of positrons like the other common ones: single close-by mature pulsars, a sum of the MW pulsar population or Super Nova Remnants (SNR). One way to improve our knowledge on this excess is to measure the direction of the flux, more precisely the anisotropy, with IACTs, thanks to their large effective area. Moreover, the smoking gun for WIMPs annihilation comes from an antideuteron excess, that could be detected by AMS-02, even if the most sensitive future detector is the balloon borne General Antiparticle Spectrometer (GAPS).

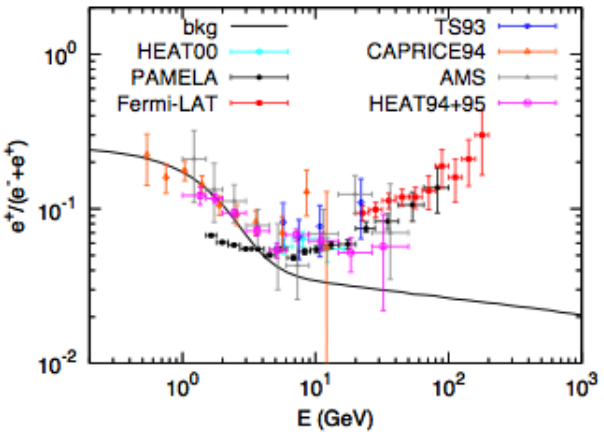

Figure 13: Positron fraction $\phi(e^+)/(\phi(e^-)+\phi(e^+))$. Credits: [11].

[14]This quantity is proportional to the product of the charged particle energy analyzer's entrance aperture area and it's solid angle of acceptance. So, the sensitivity of the instruments is proportional to it. [24]

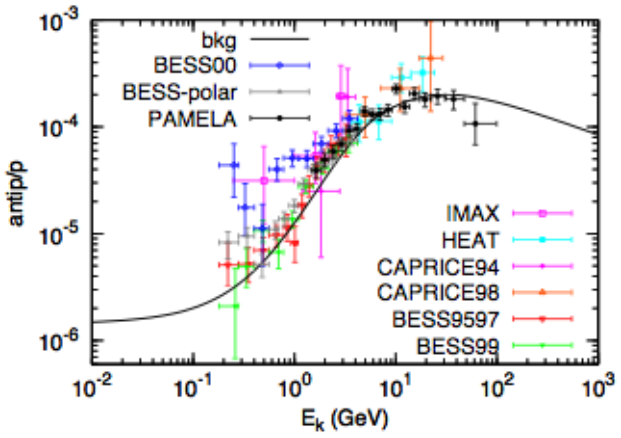

Figure 14: Antiproton excess $\phi(\overline{p})/\phi(p)$. Credits: [11].

The last indirect search for DM concerns neutrinos mainly coming from the Sun, as WIMPs are captured from it by scattering. Since the Sun is dominated by hydrogen, these neutrinos searches are very sensitive to the SD part of the WIMP-nucleon cross section, main subject of direct detection experiments and for this reason compared to IceCube (situated in the south-pole) and ANTARES (situated in the Mediterranean sea, near Toulon, France) results. For masses above 200 GeV and assuming an annihilation into b-quarks, the IceCube constraints are a factor of 2 better than COUPP, that is the most sensitive experiment of direct detection, while for annihilations into τ-quarks are up to 2 decades better.

In the following chapter I will concentrate specially on the description of MAGIC telescopes, the experiment with which had been done the measurements used for the analysis of this thesis.

3 MAGIC

MAGIC (Major Atmospheric Gamma Imaging Cherenkov telescope) is an experiment supported by an international collaboration consisting of a group of more than 150 members of different nationalities, mainly Italian, Spanish and German. After the inauguration of the first telescope MAGIC I in 2004, the system worked for five years and became, in 2009, a stereoscopic system composed of two IACTs, at a distance of $\sim$ 85 m each other. The MAGIC site include also a Counting House (CH), where the electronics and the remote controls are installed.

Figure 15: Geographical position of the island of La Palma and of the telescopes in the island.

The experiment is located at the Roque de los Muchachos, on the Canary Island of La Palma (Fig.15), at an altitude of 2235 m a.s.l. (28.8° N, 17.8° W). The choice of this site is due to the excellent weather conditions, among the best in the world (the temperature varies from a minimum of -8°C, in January/February, to a maximum of 26°C during the summer), even if occasional strong winds (from the Northern sector of the island, but the storms come from South-East), winter snowfalls, calima[15] and high humidity demand a strong technical effort to prevent damaging and ageing. Furthermore, the particular microclimate of the island causes the formation of the clouds at low altitude (between 1000 m and 2000 m) and so the altitude of the volcano (la Caldera del Taburiente, 2423m a.s.l. at the Roque de los Muchachos) permits to escape a bit from them and the laws in force in the area together with the specific position (the observatory is at the center of a nature reserve) reduce the light pollution almost to zero, improving the quality of the data.

3.1 MAGIC properties

As the other IACTs, these telescopes are designed to measure Cherenkov light from air showers initiated by gamma rays (see appendices A anb B for more details), precious font of information for Astroparticle Physics, Astrophysics and Astronomy, in the VHE regime. In particular, a purpose of MAGIC, more sensitive to low energy EM showers than the other IACTs, is to fulfill the gap existing between satellite gamma ray detectors (that can go up to some 10 GeV energy) and Cherenkov telescopes (that presently

[15] An ultra-thin Saharan sand transported by the wind from Africa which, for some days a year, fill the entire sky.

start at $\gtrsim$ 100 GeV); in fact, it works from around 50 GeV as threshold trigger energy (an analysis threshold of $\sim$ 70 GeV at small zenith angle), to more than 50 TeV in normal trigger mode.
Among the three major gamma-ray telescopes that work nowadays (H.E.S.S., VERITAS and MAGIC), MAGIC is the one that can observe farthest sources and it is also in communication with the space satellites to detect Gamma Ray Bursts (GRBs)[16]. When one of the detectors placed on a satellite detects an interesting gamma-ray event, it transmits the coordinates to the ground immediately. The two MAGIC telescopes, thanks to their fast repositioning speed, are able to set themselves to the exact direction of the source of radiation in an average time of 40 s.
From the technological point of view, "Any sufficiently advanced technology is indistinguishable from magic" (Arthur C. Clarke): the detectors use the know-how of techniques taken from accelerator experiments that allow to economically build devices of great performance and complexity, computers and networks provide sufficient capacity to record and reconstruct large volumes of data and find their interrelations. Let us see in detail the properties of the system.

3.1.1 Telescope Frame

The architecture of the two telescopes aims to reach the best mobility and the minimum weight possible and a good resistance against environmental impact. Their structure (Fig.16) consists of a very lightweight space frame made of reinforced carbon fiber tubes (Carbon Fiber Reinforced Plastic, CFRP) joined by aluminum knots, which results in a strong and light structure of a total weight of $\sim$ 5.5 tons for the mirror dish support. Thanks to the lightness, it is possible to have fast movements to follow up observations of GRBs, but it is necessary to have also an Automatic Mirror Control (AMC) to maintain the best possible optical point spread function (PSF) at different zenith angles of observations [3]. In fact, the AMC corrects small deformations of the mirror support dish during telescope positioning and tracking, moving the panels supporting the mirrors. The alt-azimuth

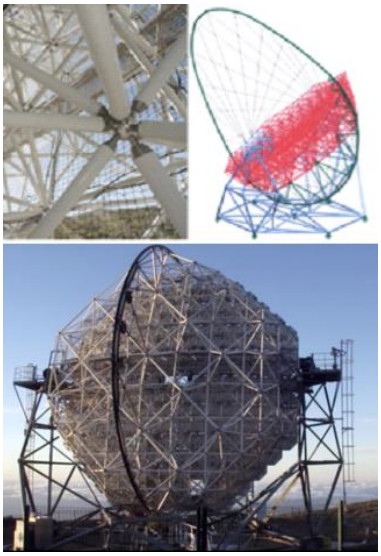

Figure 16: Illustration of the MAGIC telescope frame. *Up left:* telescopes knots. *Up right:* scheme of the MAGIC frame. *Down:* picture of the MAGIC frame Credits: [30], Adiv Gonzales Muñoz.

[16]The GRBs are violent emissions of gamma rays at VHE that last few seconds and of which we don't know the origin thoroughly.

mounting of the two telescopes, on a circular rail of 19 m ø, allows both movement in azimuth and in altitude thanks to three driving motors, each of a maximum power of 1 kW, moving a total weight of 64 ton in azimuth and 20 ton in altitude. In conclusion, the telescope can be moved from 99° to −72° in declination and from −89° to 318° in azimuth and the angular positions are controlled by absolute shaft-encoders of 14-bit precision/360°. The starguider system, in addition to the encoders, monitors the exact pointing positions and correct eventual mispointings using a sensitive CCD camera, which is mounted in the center of the telescope dish and measures the differences between stellar positions by comparing the CCD images with those recorded in standard star catalog.

3.1.2 Reflector

Figure 17: Image of the MAGIC II reflector. Credits: Adiv Gonzales Muñoz

The reflective plane of the two telescopes is a parabolic octagonal surface of ~ 236 m^2 of area, as you can see in Fig.17, focused at 10 km([17]) and of 17 m ø, chosen to preserve the temporal structure of a Cherenkov light pulse reflected on the camera. This choice leads to an improvement of the signal-to-noise ratio, thanks to a reduction of the background signals, and to a narrowing of the integration window. The focal-to-diameter ratio results to be $f/D = 1.03$ and, even if the parabolic dish presents the coma and the astigmatism as aberrations, it is the best surface focusing light that comes from infinity at a vertical incidence, at least in the center of the dish. Nevertheless, the shape of the mirrors that tessellate the telescopes is spherical, with a radius of curvature increasing from the center of the dish (33.9 m) to the edges (36.4 m) to approximate the overall parabolic shape.
Despite these common characteristics, the dishes of the two telescopes present different configurations.

[17] Position where you can find the maximum light-intensity of a shower.

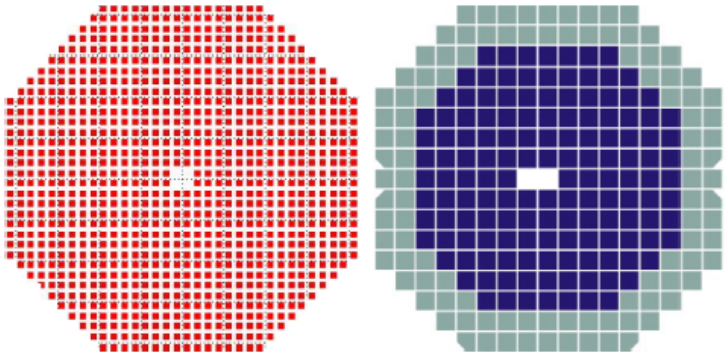

Figure 18: Scheme of the MAGIC reflectors. *Left*: MAGIC I reflector. Right:MAGIC II reflector. Credits: [30].

MAGIC I reflector is segmented with 964 squared mirrors (49.5×49.5 cm) attached in groups of 3 or 4 per each support panel (in total 247), depending on the position in the reflector frame, as shown in Fig.18. These mirrors are sandwich structure of aluminium components assembled: into the Al box an Al honeycomb spacer and a heating printed circuit board (PCB)[18], switched on in cases of dew or ice deposits on the mirrors (the total power consumption for heating the entire reflector is 40 kW), are glued, and the whole sandwich is closed with a diamond-milled Al skin, resulting in a rigid and lightweight mirror facet. In the end, to protect the reflective surface against mechanical and chemical degradation, a thin quartz layer has been deposited on the mirror surface. As far as the MAGIC II reflector regards, two different tipes of mirror have been used. 143 all-aluminium mirrors, slightly different from that of MAGIC I for the method used in the construction (used a mold for the preshape of the mirror), with a surface of 1 m^2 cover the inner part of the dish, while the outer region is tessellated with 104 glass mirrors, all directly mounted on the reflector frame (withouth using support panels). The latter ones are composite glass mirrors produced via the cold slumping technique, i.e. the assembly of the components using a vacuum suction. In conclusion, we have three kind of mirrors: the first ones, of MAGIC I, present a high surface reflectance ($85 - 90\%$), a small surface roughness (below 10 RMS) and a PSF[19] less than 1 cm; the second ones, the alluminium mirrors of MAGIC II, have more or less the same surface reflectance, but an improvement has been reached in the focusing power, being around 0.5 mrad for a point-like source; finally, the third ones, with a surface reflectance of 90% and a roughness of around 2 nm , have a less pronounced focusing power, around 2 mrad.

[18]This PCB is not present in all mirrors as some of them have been replaced with new ones.
[19]Point Spread Function: defined as the radius of 90% light containment.

3.1.3 Camera

One of the key elements of the γ-sensitivity of MAGIC is the camera, that is kept in the focus of the reflector and it is supported by a tubular arch of aluminum, stabilized by thin steel cables and counter weights.
In its first version, MAGIC I camera, of hexagonal shape (114×104 cm) and covering a field-of-view (FoV) of 3.6°, was composed of 576 different pixels: 396 1" diameter ET 9116A PMTs covering the inner section up to 1.2° and 180 0.2° FoV PMTs of 1.5"diameter of ET 9117A type arranged in concentric rings in the outer part of the camera. Given that the photocatode of the PMTs is of spherical shape, to achieve the maximum active camera area, avoiding dead space between the densely packed PMTs, and rejecting background light, hexagonal light concentrators similar to Winston cones[20] have been placed in front of the photodetector matrix. Moreover, to enhance the quantum efficiency (QE)[21], it has been used a laquer doped with P-Therphenyl[22], that shifts the short wave UV component of the Cherenkov light into the spectral range of larger sensitivity of the PMTs. With this technique, the QE increases from $\sim 20\%$ to $\sim 30\%$ at shorter wavelenghts.
In 2011/2012 the MAGIC committee decided to begin an upgrade program to improve and unify the stereoscopic system of the two telescopes, making the two telescopes as similar as possible. Among the main hardware parts that have been upgraded, we can find a new MAGIC I camera, that made this one similar to MAGIC II one, having the quality to be composed of small pixels only, that allow a better determination of the image parameters. In fact, the old pixels have been replaced with 1039 PMTs from Hamamatsu, type R10408, 1" diameter, with a hemispherical photocatode and 6 dinodes. These PMTs can reach a peak QE of 34% in the UV band, providing a fast response of the order of ~ 1 ns FWHM, and are grouped into cluster of hexagonal shape containing 7 pixels each. The configuration adopted permit an easy exchange of broken clusters and eases potential upgrades. The main difference from the MAGIC II camera pixels is the PMTs gain. A half of the new PMTs of MAGIC I camera, at the same voltage [3] of MAGIC II camera, have an higher gain (4.5×10^4) than the others (3.0×10^4) and than that of MAGIC II (3.0×10^4). The intrinsic spread in gain observed in MAGIC II PMTs, coming from the manufacturing processes, led to choose for the high gain PMTs of MAGIC I camera in order to facilitate the flatfielding procedure, needed to calibrate the signal (i.e. to have the same photon number at the entrance of each PMTs), and to counter act ageing effects [7]. Moreover, this new configuration allowed the testing of Silicon Photo-multipliers (SiPM), leading to the installation of

[20] Non- imaging light collectors, i.e. instruments that do not attempt to form an image of the source, but to optimize the radiative transfer from a source to the target, in the shape of an off-axis parabola of revolution with a reflective inner surface (in this case they are covered with an alluminate-Mylar foil with an average reflectivity of 85%), that maximize the collection of the incoming rays allowing off-axis rays to make multiple reflections before reaching the exit aperture.

[21] Very important property of a detector that reports the photon detection efficiency.

[22] It is one of the three isomers of the therphenyl (a group of aromatic hydrocarbons consisting of a chain of three benzene rings) industrially used as dye for dye laser or as ingredient for sunscreens.

a cluster in the outer region of MAGIC II camera, that have higher sensitivity than present PMTs.

3.2 MAGIC Data Aquisition

MAGIC telescopes work taking data divided into subruns, grouped into runs, of ~ 20 min each. During this time, we can found three different kind of events: pedestal events, calibration events and data events. The first ones are events recorded using random trigger, with a fixed trigger frequency of 1 kHz, with null probability of recording atmospheric shower events. Their purpose is to define the electronic noise of the readout system in order to make the mean cell offset calibration, applied online by the DAQ (Data Aquisition) program (see the following paragraphs for a more detailed description). The calibration runs are of two different types: the extensive ones are taken at the beginning of the observation of a new source during each night and allow the flat-fielding of the camera through the F-factor method[23], while the interleaved ones monitors the correction factor during time, looking at the gain in the readout chain of the individual channels with a frequency of 25 Hz. Assuming that the calibration of chip response is required, besides the mean cell offset calibration, we need a readout time lapse correction and a signal arrival time calibration to obtain optimal results as far as the noise and time resolution regard; but let see in detail how proceed the telescopes operations and the data flows (Fig.19).

[23]Method that consists in multiplying each PMT of the camera for a corrective factor, using an intrinsic PMT parameter, in order to artificially flat-field the camera, giving the fact that there is an inhomogeneous response of the camera to gamma rays. This fact can come from different gains in the electronic chain, different electronic noise levels or different levels of the Night Sky Background (NSB), due to the presence of stars in the FoV.

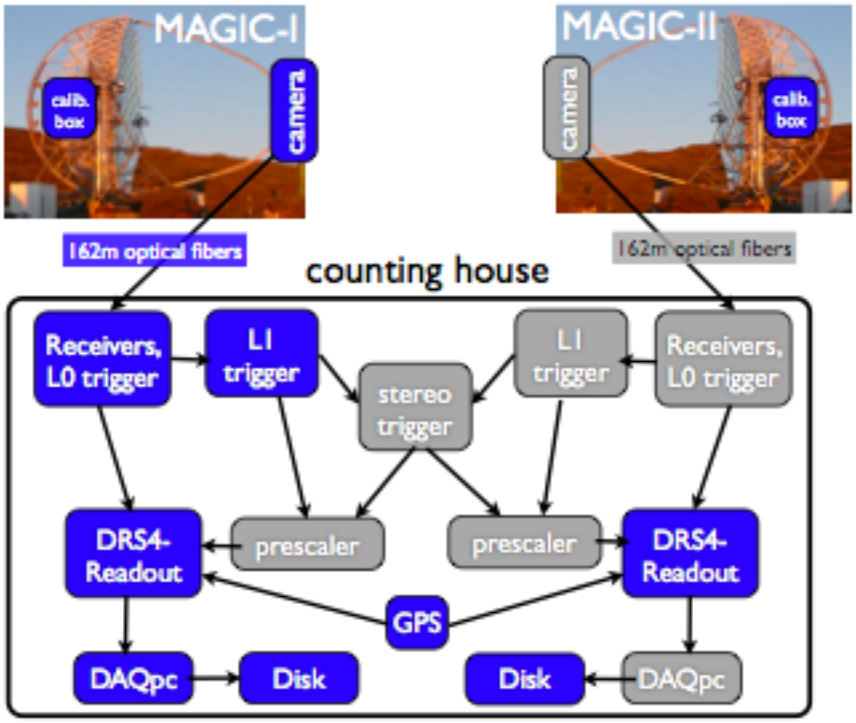

Figure 19: Scheme of the readout and trigger of the MAGIC telescopes. The parts changed with the upgrade are contained in the blue boxes. Credits: [3].

3.2.1 Readout Chain

The short duration of the Cherenkov light signals requires a very fast readout electronics after the acquisition of the analog signals with the camera PMTs. Subsequently to the upgrade mentioned previously, the analog signal, whose amplitude depends on the intensity of the Cherenkov light, is amplified by an ultra-fast and low-noise preamplifier, transformed into an optical signal by Vertical Cavity Surface Emitting Lasers (VCSELs) and transmitted to the CH (80 m far away), passing through $\sim$ 162 m long optical fibers[24] grouped in 19 bundles per telescope with 72 fibers each. This bundles allow a better handling and ensure mechanical rigidity (they protect the fibers from breaking and from the strong sun UV radiation) being protected by a UV resistant PVC cover. Nevertheless, the main important thing to keep in mind is to maintain the same arrival time between individual channels (there is a spread due to different times of flight in the optical fibers) and for this reason it was developed a special setup, so the resulting spread in propagation time became 138 ps (RMS). This last is corrected offline using calibration light pulses.

[24]Their usage gives a low pulse dispersion and attenuation and protect the signal inside from the external electromagnetic noise.

When the signals arrive at the electronic room of the CH they meet the Magic Optical Nano-Second Trigger and Event Receiver (MONSTER boards), that reconverts the signal to analog electrical ones, splits them into two halves, one for the digitization electronics and one for the trigger (see section 3.2.2 for more details), and generate the level-0 (L0) individual pixel trigger signal using discriminators. The second main part of the readout electronics, the digitization ones, is composed of a total of 48 Domino Ring Sampler version 4 (DRS4) mezzanines installed in each readout, reaching 1152 readable channels, that are sufficient to cover all the pixels of the camera. These cips are ultra-fast analog memories read out, at lower speed, by a 14-bit nominal resolution analog-to-digital converter (ADC) and have a sampling frequency of 2 GSamples/s, linear response in an input range of 1 V and a negligible dead time of 27 μs. The choice of these DRS4 was made with the upgrade in order to maintain the performance of the previous readout based on MUX-FADCs (multiplexed system and Flash Analog-to-Digital Converters) for MAGIC I, to improve the readout chain for MAGIC II (previously based on DRS2, that gave a dead time worse of 1% than this new one), but increasing the charge resolution, reducing costs and save space. This last point is very important because of the fact that the electronic room in the CH would not be able to host a readout of more than 2000 channels in the previous configuration.

3.2.2 Trigger System

MAGIC trigger is a system used to reject the storage of background events coming from the Night Sky Background (NSB) optimizing the data acquisition. In both telescopes, it covers 547 inner pixels of the camera (MAGIC I trigger area has become similar to that of MAGIC II with the upgrade), i.e. a FoV of 2.5° diameter, allowing the study of extended sources with angular sizes $\geq 0.3°$. The trigger follows three steps:

- **Level zero (L0) trigger:** This is a simple amplitude discriminator that operates on each pixel individually cutting signals that don't get over the Discriminator Threshold (DT), set at 4.25 phe in the standard mode, automatically adjusted by the Individual Pixel Rate Control (IPRC) for every pixel in the trigger region.

- **Level one (L1) trigger:** The signal that passed the level zero of the trigger arrives at this level after its width and delay are set individually, in order to minimize the spread of arrival times for contemporaneous signals. At this step, the signal encounters a digital filter arranged in 19 overlapping macrocells of 37 pixels each (36 active and one blind), as you can see in Fig.20.

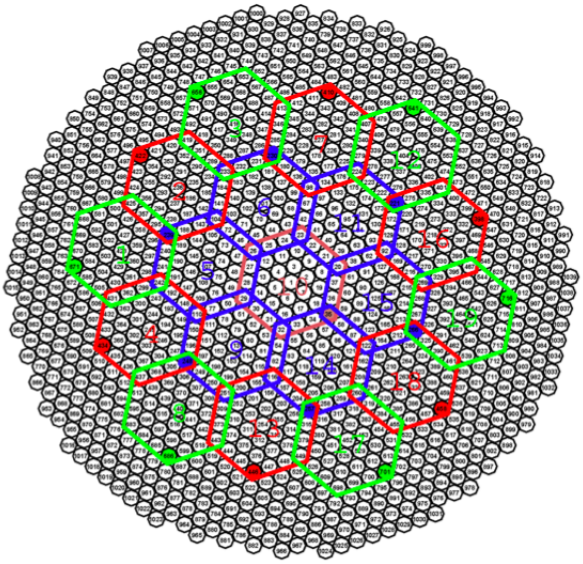

Figure 20: Configuration of the MAGIC trigger area. Credits: [17].

This individual telescope trigger is based on the next-neighbour (NN) logic, i.e. it looks for next neighbors pixels with a current that exceeds the DT in a tight time window ($\sim$ 7 ns effective width) in any of the cluster of channels defined previously, with several logic patterns implemented: 2NN, 3NN, 4NN and 5NN, as you can see in the following image.

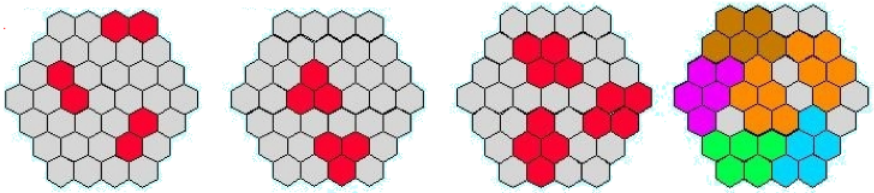

Figure 21: NN logic of 2, 3, 4 and 5 pixels. Credits: [17].

When the multiplicity condition (selected remotely by the software) is satisfied by any of the macrocells, a signal with a width of $\sim$ 25 ns is sent to the following trigger level (the decision is taken in less than80 ns), after being corrected in width and delayed by the multi-thread C-program HYDRA (that runs as a part of the MIR), to take into account the differences in the arrival times of the Cherenkov light events, due to the azimuth and zenith orientation of the telescopes.

- **Level three (L3) trigger:** This last step of the trigger chain it is due to the stereo configuration of the two telescopes, because it rejects events that have been triggered by only one of the two telescopes.

Other two types of trigger implemented and now in testing phase could substitute L1 trigger and L3 trigger respectively. The SumTrigger is based on 55 hexagonal overlapping macrocells each containing 19 PMTs, for a total of 529 pixels. Once a trigger signal comes from a macrocell, the final trigger is the global OR of the local macrocells trigger. The advantages of this configuration let to relax topological constraints and to put discriminator at the end of the chain, proving better performances in the domain below $50-60$ GeV, when the events become small. The possible replacement of the L3 trigger is the TOPO Trigger, that thanks to the topological discrimination of events, allows a one order of magnitude decrease of the accidental events triggering MAGIC stereo system.

3.2.3 Calibration

The system of calibration of the MAGIC telescopes is based on a calibration box that illuminates uniformly the PMTs camera with well-characterized light pulses of differents intensities in order to convert the data taken with the DRS4 into informations about the incident Cherenkov light flux. Originally, MAGIC I calibration box was composed of fast-emitting LEDs with pulses of $3-4$ ns FWHM, while MAGIC II of a system with a passively Q-switched Nd:YAG laser producing pulses of 0.4 ns. After an improvement of MAGIC I calibration box, with the upgrade in 2013, both calibration boxes have been changed. It has been proven that the laser-based system is superior to the LED-based system for the larger dynamic range and for the shorter light-pulses (< 2 ns FWHM) , that are more similar to the ones produced by the Cherenkov flashes from extended air showers. So, it has been decided to install 62 calibration boxes (each one controlling 4 mirrors), similar to that of MAGIC II, with a humidity sensor inside the boxes, a system that shows the laser status, a heated system to avoid water condensation and a photodiode to monitor the laser light output. Moreover, as the light intensity is adjusted through the use of a calibrated optical filter and the uniformity is achieved through the use of an Ulbright sphere, both these quantity have been improved, reaching a variation of the telescope illumination $< 2\%$.

4 PERSEUS

As shown in chapter 2, IACTs are instruments that study VHE gamma-rays and they are more sensitive at energies from few tens of GeV to a hundred TeV. Pointing the attention in particular to DM particles, gamma-rays are one of the possible products of their annihilation/decay. The corresponding spectrum is a continuum with a steep exponential cutoff at the DM particle mass. To measure these gamma-rays, one has to point the instruments where DM is concentrated and, possibly, to nearby sources. The reasons for these requirements are that the flux of gamma-rays from annihilation (decay) of DM goes like $\Phi \propto \rho^2$ ($\Phi \propto \rho$) and decreases with the square of the distance to the target. Keeping in consideration these conditions, different are the possible targets for DM indirect searches with IACTs. One of the closest and more DM dominated is the Galactic Center (GC), sited 8.5 kpc away from us. In addition to the expected DM component, it contains a lot of astrophysical sources that hide the possible DM signal, emitting radiation at least one order of magnitude bigger than DM one. Thus, the only way to unveil possible spectral features that could be sign of DM is to make accurate and prolonged observations of the GC. Another site of interest for DM studies are the intermediate mass black holes (IMBH), that have a mass between $\sim 10^2 M_\odot$ (mass of the stellar mini black holes) and $\sim 10^6 M_\odot$ (mass of the supermassive black holes, SMBH). IMBH are peculiar objects, because they are expected to have a very clumpy DM distribution around them, due to the interplay between the small baryonic content and the strong gravitational field around the BH (Black Hole). For this reason, in case of annihilating DM, the annihilation signal is expected to be bright, but also these objects have not a clear identification in the sky. The other two sites where to look indirectly for DM are complementary in term of searches: Dwarf Spheroidal Galaxies (dSphs) and galaxy clusters. The formers are satellites orbiting in the gravitational field of a larger host galaxy (including our Milky Way) and are the most DM-dominated systems known in the Universe ($M/L^{(25)} \sim 1000$ for some recently discovered dSphs). For thie reason and for the fact that they are rather close by objects, they are very good candidate for DM searches with IACTs. On the opposite, galaxy clusters are very far-away objects (Mpc scale compared to the kpc scale of the dSphs). However, most of the matter in the cluster is believed to be made of DM. If one wants to compare the two classes of targets, one can say that dSphs are more attracting targets than galaxy clusters if the DM is annihilating, because in this situation the DM concentration matters. On the other hand, in case of decaying DM, galaxy clusters are more attractive, because, despite being far, they contain very large DM content. In addition, compared to the angular resolution of IACTs, of about 0.1 deg, dSphs appear as rather point-like sources, while cluster are extended - in terms of expected DM emission. One last point, quite debated in the past, is the different contribution in terms of DM substructures (see §4.3 for more details) among these two targets. All these considerations are pointed out looking at Fig.22, in which it is shown a comparison among the fluxes of three

[25] Quotient between the total mass of a spatial volume and its luminosity reported using the value calculated for the Sun as a baseline ratio, that is $M_\odot/L_\odot = 5133$ kg/W.

MW's dSphs (e.g. Willman 1, Segue 1, UMi-A) and those of the clusters with highest gamma-ray fluxes known (Virgo, Fornax and Ophiuchus). One can notice that, even considering the effect of substructures that boosts the fluxes of galaxy clusters in the figure on the bottom, at small angles of observation the flux of dSphs is higher than that of galaxy clusters, while, at higher angles, galaxy clusters fluxes are predominant, showing then the complementarity of the two kind of sources for indirect DM searches.

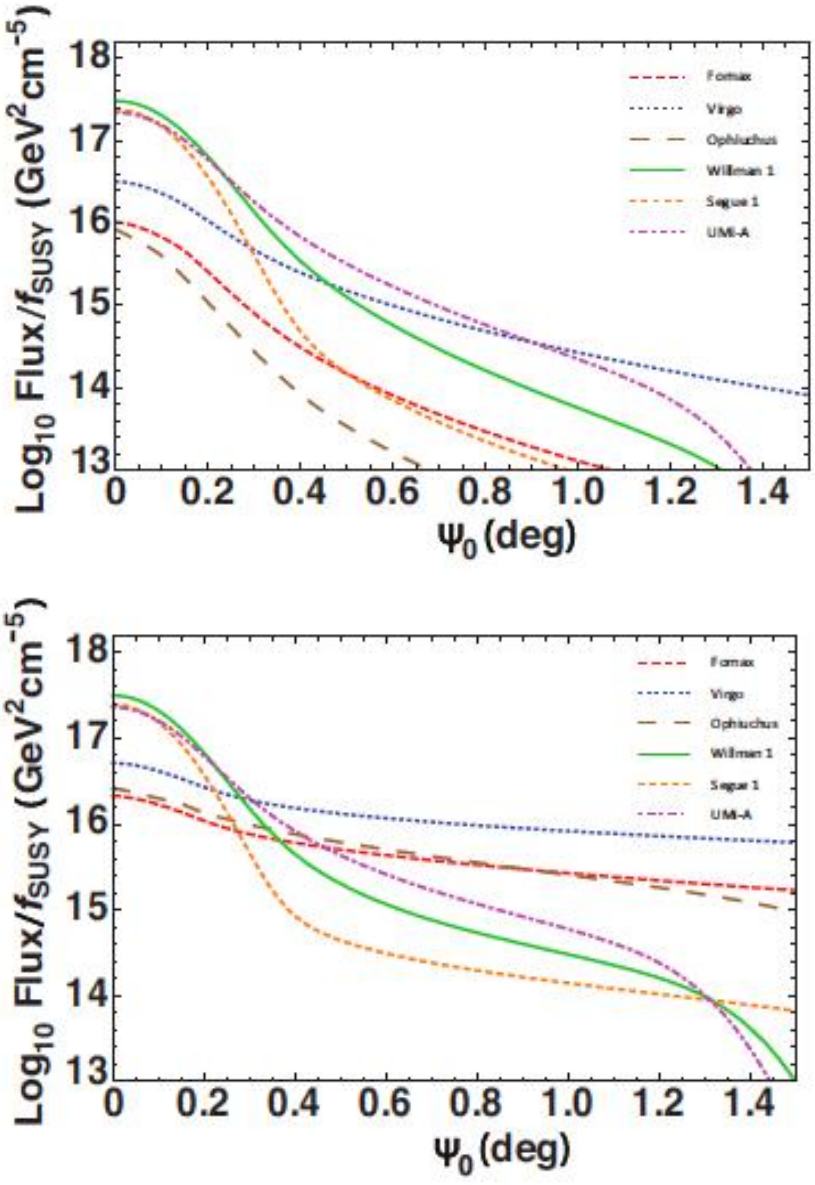

Figure 22: Comparison of the fluxes among dSphs and galaxy clusters, without substructures (*top*) and with them (*bottom*). Credits: [29].

4.1 Flux of gamma-rays from decaying DM

Considering gamma-rays coming from the decay of DM particles, the differential flux can be described as the product of a particle physics (PP) factor and an astrophysical factor (J):

$$\frac{d\Phi_\gamma}{dE} = \frac{d\Phi^{PP}}{dE} \times J(\Omega)$$

where

$$\frac{d\Phi^{PP}}{dE} = \frac{1}{4\pi m_{DM}\tau_{DM}} \frac{dN_\gamma}{dE}$$

with m_{DM} and τ_{DM} the mass and the mean lifetime of the DM particle respectively, and dN_γ/dE the number of photons found in the prompt products of the DM decay. As one can see, this term is determined by the nature of the DM particle, while the astrophysical factor (J-factor) depends on DM density distribution and is given by:

$$J(\Omega) = \int_\Omega d\omega \int_{los} \rho(r(s))ds$$

where Ω is the solid angle, *los* is the line of sight, i.e. the straight line connecting the source to the observer[26], and $\rho(r(s))$ is the density of DM in the cluster in function of the distance r from the center. This distance is given by:

$$r(s,\psi) = \sqrt{s^2 + D^2 - 2sD\cos\psi}$$

with s distance from the observer to a point lying on the line of sigth and corresponding to a relative distance r, D distance from the center of the source to the Earth and $\cos\psi = \cos b \cos l$, where b and l are the galactic latitude and longitude respectively.

4.2 Introduction to Galaxy Clusters

As introduced at the beginning of this chapter, clusters of galaxies are optimal target for DM decay searches: they are composed of DM for the 80% of their mass. Clusters of galaxies are the largest and most massive gravitationally bound systems existing in the Universe. In addition to DM, their matter content is shared between 5% in galaxies and 15% in gas, and they can reach masses of $10^{14} - 10^{15}$ $M_\odot$ and radii of few Mpc. Cluster of galaxies are the latest stage of structure formation, according to the concordance with the cosmological model, that foresee a bottom-up scenario, where larger structures result from the merging of smaller structures. Nowadays, they are object in virial equilibrium, also termed relaxed. During the merging and accretion processes, energy emissions of the order of the final gas binding energy ($\sim 3 \times (10^{61} - 10^{63})$ erg) have been dissipated with rates of $L \sim (10^{45} - 10^{47})$ erg s^{-1} and a small fraction of the energy released could have been channeled into non-thermal electrons

[26] Along the line of sight, the observer is unable to distinguish gamma rays coming from the same direction but at different distances (neglecting absorption and diffraction effects).

and protons accelerated at high energies, allowing a detection of them in the gamma-ray regime. Moreover, the ICM (Intra Cluster Medium), being a heated gas between galaxies at a temperature of $7-9$ keV, can function as an efficient energy reservoir and should be also an acceleration site for relativistic protons and heavier relativistic nuclei. These ones, as they are heavier than electrons, have longer cooling time, during which they interact inelastically with ambient gas protons of the ICM and generate subsequent pion decays. The electrons and positrons found in such pion decays can also, in turn, produce gamma radiation through the synchrotron mechanism in the magnetic fields present. In conclusion, galaxy clusters are expected to emit a large amount of gamma-rays having different origin, but those we are interested in are gamma-ray signals coming from DM decays, in particular from Perseus galaxy cluster.

4.3 Perseus Galaxy Cluster

Perseus is a cool-core cluster (known also as Abell426) of extragalactic origin, being at a distance of 77.7 Mpc ($z = 0.018$) from the Earth. It is the brightest X-ray cluster, having a luminosity of $L_X = 8.3 \times 10^{44}$erg s^{-1} in the soft X-ray band from 0.1 keV to 2.4 keV, and it presents a high central gas density and a luminous radio mini-halo, that has an extension of 200 kpc. An hypothesis on the nature of the halo is that it had been generated by secondary electrons/positrons created in hadronic cosmic ray (CR) interactions (hadronic model).

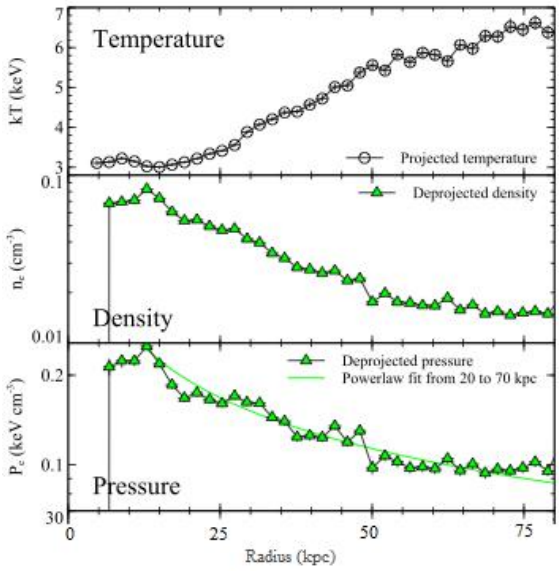

Figure 23: Measured temperature, density and pressure in the Perseus cluster. Credits: [19].

Another possible gamma-ray emission can be expected in the re-acceleration model: states of powerful ICM turbulence re-accelerate CR electrons/positrons (maintained at

around 100 MeV of energy by particle-plasma wave interactions at a rate faster than the cooling process) at sufficient energy to produce observable radio emission. Keeping our attention on the hadronic model, then, we notice that limits on the gamma ray emission, in the hadronic acceleration model, give limits on the intra-cluster magnetic field, that is supposed to be $B \sim 20\,\mu$G from Faraday rotation measurements[27] (MAGIC analysis on Perseus cluster [6]).
Looking in particular at the conformation of Perseus cluster, only two are the galaxies we are able to observe nowadays through VHE gamma-rays: NGC1275 radio galaxy is sited in the center of the cluster and IC310 is 0.6° away. The inclination angle of NGC1275 jet, being an Active Galactic Nuclei (AGN), increases from $10° - 20°$ at milliarcsecond scales up to $40° - 60°$ at arcsecond scales. Fig. 24 shows two skymaps of the Perseus galaxy cluster taken with the MAGIC telescopes, one at energies larger than 150 GeV (left) and one at energies larger than 630 GeV (right). One can see that NGC1275 (at the center of the image) is present only in the left-hand image. This is due to the soft-ness of its photon spectrum, which rapidly fades off at increasing energies. On the other hand, IC310 is present in both images. This is due to the hard-ness of its spectrum. IC310 is thought to be a so-called head-tail radio galaxy[28] that hosts a very peculiar black hole [4].

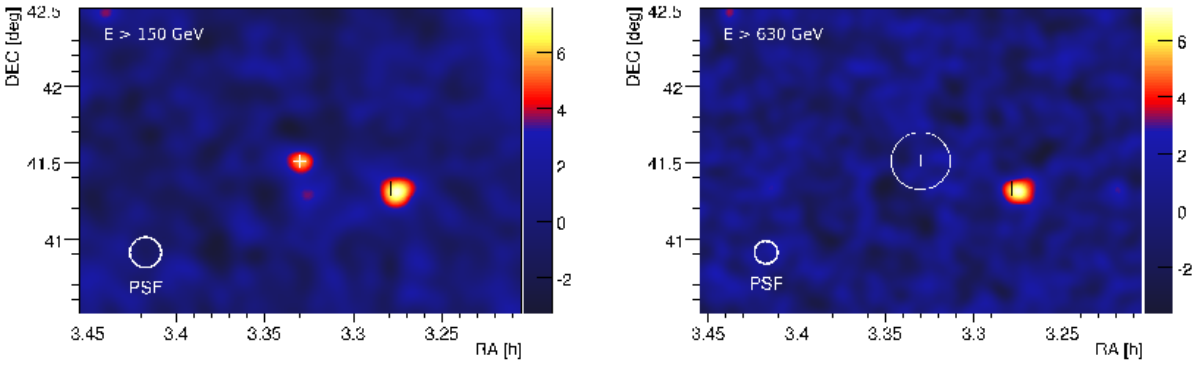

Figure 24: Skymaps of Perseus sky at different energy theresholds; 150 GeV for the left plot and 630 GeV for the right one. Credits: [6].

Perseus has been chosen as a candidate for the observations with MAGIC (more than 300 hours of data taking in the years 2009-2015) principally because of its expected high gamma-ray emission induced by the hadronic or leptonic cosmic rays acceleration scenarios. As for DM expected signal, it is not the cluster with the highest expectation

[27]Since the emission at radio wavelengths is often due to synchrotron emission, the radiation is linearly polarized with the electric-field vectors, but comes to the observer with different polarizations because of the fact that it propagates through the interstellar medium. Through this effect, called Faraday rotation, the astronomers are able to estimate magnetic fields in the ICM, along the line of sight.

[28]Systems that have a bright source accompained by a tail or tails that appear swept back by their interactions with the intergalactic gas, that is cooler and more stationary.

(Fornax is the optimal cluster for DM searches, but it is located in the Southern hemisphere), although its DM content is large enough to guarantee interest in this source. Moreover, in particular for this thesis, Perseus has been taken into account as DM target in the context of decaying DM. As already mentioned, this is due to the fact that, in case of annihilating DM, the expected signal from Perseus is extremely weak, due to the large distance, unless a contribution from substructures, that boost the intrinsic signal of a 1000 times, is considered. The substructures had been originated by the merging processes of little DM haloes into bigger ones and they were thought to boost the DM annihilation flux considerably, as the signal depends on the DM density squared. Consequently, the semianalytical model 3K10, developed by Kamionkowsky, Koushiappas and Kuhlen to include substructures in the calculation of the DM annihilation flux, together with other analytical models and N-body simulations, has been used to have a realistic and precise computation of the boost factor due to substructures, that is given by:

$$B(r) = f_s e^{\Delta^2} + (1 - f_s)\frac{1+\alpha}{1-\alpha}\left[\left(\frac{\rho_{max}}{\rho(r)}\right)^{1-\alpha} - 1\right]$$

where the first term is due to the finite width of the smooth component, as f_s refers to the volume of the halo filled with this DM component with density $\rho(r)$, and the second term is due to substructures, as $(1 - f_s)$ corresponds to a high-density clumped component. α , Δ and ρ_{max} are parameters calculated from the calibration of the model through simulations [29]. Despite this, f_s is known with limited precision because of the fact that simulations are not able to resolve the whole sub-halo hierarchy. One thing should be made clear. Because of the dependence on the square of the DM density in the case of annihilating DM, it is clear that the presence of DM substructures, which are highly concentrated, strongly contribute to the total expected flux from the source. On the other hand, the same number of substructures, in case of decaying DM, do not significantly alter the total decaying-DM signal expected from Perseus, given the slower linear dependence from DM density in this scenario. Nevertheless, such boosts, despite being considered possible only few years ago, are now considered highly improbable [29].

4.4 Dark matter density profile

Around galaxies or cluster of galaxies the DM density profile is known through studies of gas emissions, members objects' velocity and velocity dispersions etc. However, all these data together does not allow to infer a very precise DM profile, because of finite resolution data, specially toward the center of the cluster. For this reason, normally, we rely on DM profile obtained with so-called N-body simulations. These are computer simulations that let a distribution of DM particle evolve through gravitational-only interactions and investigate the final stages of the development. N-body simulations are very computer-exhausting, and therefore simplifications must be used: the minimum DM mass is at about $10^4 - 10^6$ solar masses, and almost always the baryons are not

included. While the former has the consequence that we cannot investigate very small distributions of DM or short-scale effect, the second has the effect that the baryon-DM interaction is not clear. Adding baryons is not only a computer challenge because of more particles, but specially because one has to include all the physics of baryons, including stellar formation and explosion, stellar wind, tidal streaming etc. Fig.25 shows the results obtained with N-body simulations. The black curve is the NFW density profile. Adding baryons to the simulation, the central density becomes more cuspy (red curve) because of the enhancing of gravitational attraction, but a consequence of this large amount of matter are the supernovae explosions, that create an outflow of particles producing a core profile (blue curves). More baryons are added to the simulation, more supernovae explosions and more the density profile becomes a core one. One can see this looking at the three blue curves in the figure.

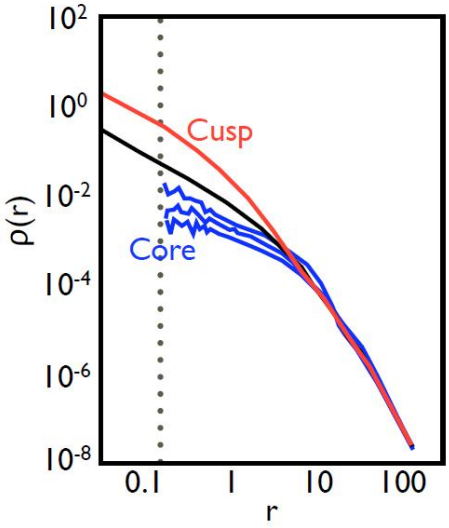

Figure 25: Cusp/Core density profiles obtained from N-body simulations. Credits: [27].

N-Body cosmological simulations give a universal formula to describe the DM density profile of gravitationally bound systems and this is given by:

$$\rho(r) = \frac{\rho_0}{\left(\frac{r}{r_s}\right)^{\gamma}\left[1+\left(\frac{r}{r_s}\right)^{\alpha}\right]^{\frac{\beta-\gamma}{\alpha}}}$$

where ρ_0 is the characteristic density of the gravitational bound system studied and r_s is its scale radius, while α, β, γ are the free parameters. By changing the free parameters, one can produce different profiles, either cuspier or more cored. For the analysis I will take in consideration the Navarro-Frenk-White (NFW) DM density profile, as it shows a good agreement with the observations. Its formula is given by:

$$\rho(r) = \frac{\rho_s}{\left(\frac{r}{r_s}\right)\left[1+\frac{r}{r_s}\right]^2}$$

in which ρ_s is a typical scale density. In particular, for Perseus galaxy cluster, the values of the parameters are: $r_s = 0.477$ Mpc and $\rho_s = 7.25 \times 10^{14} M_\odot$ Mpc^{-3}(see [29]) and the density profile results to be that one in Fig.26.

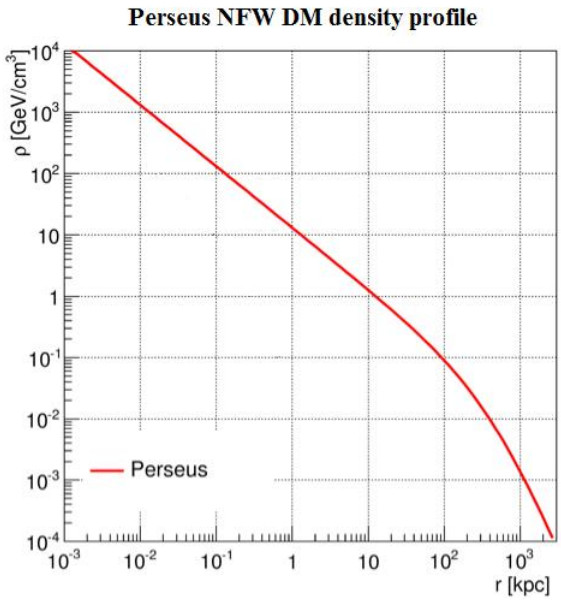

Figure 26: Perseus DM density profile using NFW formula. Credits: [Palacio private communication].

4.5 Angular Optimization

To look for the maximum number of gamma-rays produced by DM decays in Perseus galaxy cluster, keeping in consideration the instrumental and experimental limits, an optimization technique based on the angle θ (coordinate in the sky plane) has been used. The angular optimization is founded on the maximization of the following ratio:

$$Q(\theta) = \frac{N_\gamma}{\sqrt{N_{bkg}}}$$

where N_γ and N_{bkg} are the number of gammas coming from DM particles decay and from the background respectively, and $Q(\theta)$ is called Q-factor. A modeling of the background is needed in order to put in the formula the proper flux of gamma-rays obtained. The simplest approximation for the background is a uniform flux of gamma rays coming from all over the sky and, as one can write for the background flux the same expression used previously for the DM signal, the Q-factor becomes

$$Q(\theta) \propto \frac{\int_{d\Omega}\int_{los}\rho(r(s))ds}{\sqrt{\int_{d\Omega}\int_{los}ds}}.$$

One can notice that the θ value that maximizes the expression is that one that minimizes the sensitivity. The inverse proportionality can be used to calculate the sensitivity for extended sources, knowing the one of point-like sources ($\theta \approx 0.1°$). Then, taking into

account the instrument response function, the expression of the Q-factor becomes:

$$Q(\theta) \propto \frac{\int_{d\Omega}\int_{los}\rho(r(s))\epsilon_{\gamma}(\theta,\phi)ds}{\sqrt{\int_{d\Omega}\int_{los}\epsilon_{bkg}(\theta,\phi)ds}}$$

where θ, ϕ are the coordinates in the sky plane and ϵ_{γ}, ϵ_{bkg} are the signal and background efficiencies respectively. Even if the efficiencies could be thought to have different values, as, in principle, the telescopes have different efficiencies for the background and the signal region, we consider them the same quantity ϵ.
In conclusion, taking advantage of the inverse proportionality and using the Crab nebula observations to measure the efficiency, as it is the most known source, one can find an expression of this efficiency in function the angle θ. In this manner, one can optimize the Q-factor. Nevertheless, limitations on the interpretation of the optimization occurs when taking into account instrumental limits, like the angular resolution of the experimental apparatus [Palacio private communication].
As far as the analysis on Perseus cluster concerns, the signal is expected to come from an extended region, a little bit larger than the telescope PSF, and for this reason the θ angle of aperture had to be optimized, limiting the background signal. Keeping in consideration the formula for the optimization of the Q-factor written above, the angle at which the J-factor for decaying DM is maximum is at $\theta \simeq 0.35°$,as you can see in Fig.27.

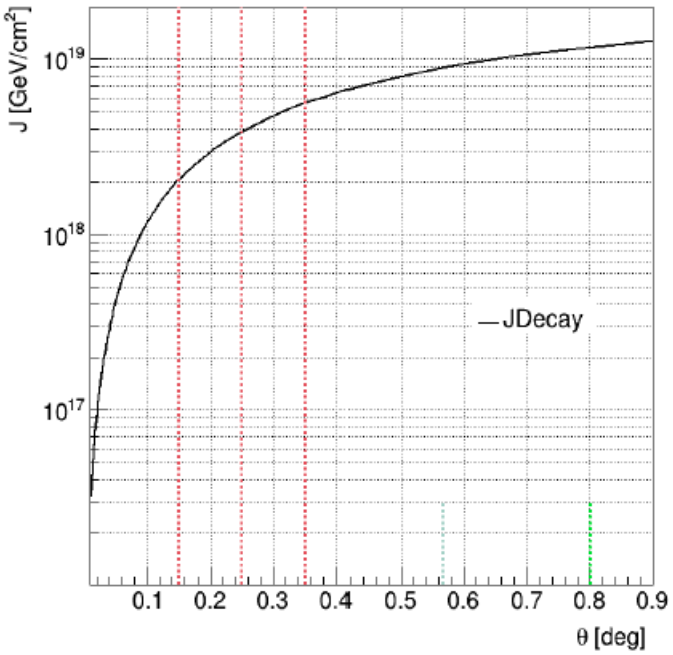

Figure 27: J-factor in function of the θ angle. The two red lines delimit the areas where the J-factors are calculated. Credits: [Palacio private communication]

In fact, for the analysis of this thesis it has not been used the total J-factor ($J_T(\theta_{min} = 0.^\circ; \theta_{max} = 0.35^\circ) = 5.63389 \times 10^{18}[\text{GeV cm}^{-2}]$), obtained integrating over the total angular extension of the object, but the J-factors calculated in the angular ranges $[0.15^\circ, 0.25^\circ]$ and $[0.25^\circ, 0.35^\circ]$, to maximize the number of events respect to the background and to exclude the NGC1275 source from the analysis, as it gives us nuisance signals. In particular, the values obtained for the J-factors in different rings around the center of the source are the following (for more details see the following chapter):

$$J(\theta_{min} = 0.15^\circ; \theta_{max} = 0.25^\circ) = 1.82599 \times 10^{18}[\text{GeV cm}^{-2}]$$

$$J(\theta_{min} = 0.25^\circ; \theta_{max} = 0.35^\circ) = 1.75580 \times 10^{18}[\text{GeV cm}^{-2}]$$

5 PERSEUS RECONSTRUCTION

The observations done on Perseus galaxy cluster, located at RA= 3.3299 h and DEC= 41.5103 deg, have not the only purpose of indirect search of DM, but they were also finalized to study the cluster in term of cosmic ray emission, as well as because of the presence of active galactic nuclei in the Field of View (FOV). The global data sample acquired by MAGIC covers more than 300 h, pointing the telescopes on different pointing positions: one to study Perseus_MA and NGC1275 and the other in a position useful to have the galaxy IC310 near our FOV, as it is a very interesting source to take into account of. In particular for this analysis, we concentrate in the period from 2013/07/27 to 2014/08/05, in which data were taken, for $\sim$ 64 hours, in wobble mode from both Peresus_MA and NGC1275 sources. Differently from ON/OFF mode, in which for a half of the observation time the telescopes point to the center of the source (ON) and for the other half to the background region (OFF) with similar zenith and azimuth angles [21], the wobble mode is a technique in which the telescopes are pointed at a fixed distance from the center of the source (in our case at 0.4°) and at a fixed angle (chosen during the proposals for the observation, based on possible peculiar sky features, e.g. presence of bright stars) and moves the telescopes of 90° each 20 minutes for 4 wobble positions or of 180° for 2 wobble positions. As one can see in Fig.28, the center for the NGC1275 observations is point (A) and has 4 wobble positions (W0.40+058, W0.40+157, W0.40+238, W0.40+337), while Perseus_MA observations have the center in point (B) and use 2 wobble positions (W0.40+108, W0.40+288). In the wobble pointing mode, all time is used to measure ON and OFF data simultaneously, except for the time used to move the telescopes that is indeed a dead time. One can observe the ON signal during every wobble position and one can calculate the OFF using a region in the camera that has the same acceptance of the ON one and that is symmetric to the source position with respect to the center of the FOV, i.e. in our case at 0.8°, as one can see in Fig.29 for the two wobble positions of Perseus_MA observations.

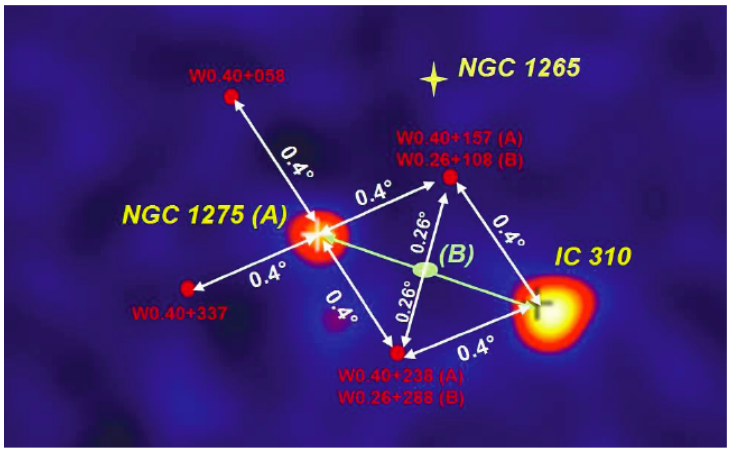

Figure 28: Wobble positions in Perseus sky. Credits: [Palacio private communication].

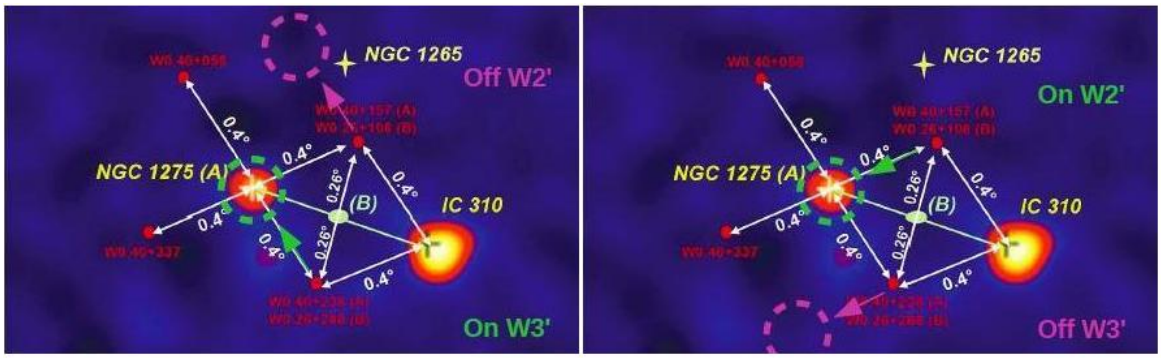

Figure 29: Off from wobble partner in Perseus observations. Credits: [Palacio private communication].

The higher is the number of the OFF regions for each wobble position and the lower is the statistical uncertainty on the OFF. This is the reason why for MAGIC observations we can have 1, 3,5 or 7 OFF regions for each wobble position. Talking about the particular case of our analysis, only one OFF region for each wobble position have been used for the observations, in order to avoid overlappings between ON and OFF regions. In fact, we could have had the overlappings using more than one OFF region for each of the 4 wobble positions, as the extension of the ON region is 0.35°, being Perseus an extended source. The optimal configuration would have been the one with a distance between the ON and OFF regions for each wobble position at least as large as the PSF, that is 0.1°. Moreover, considering both targets of the observations, one can see in the plot of Fig.30 that the zenith range of our datasample ranges from $\sim 5°$ to $\sim 60°$.

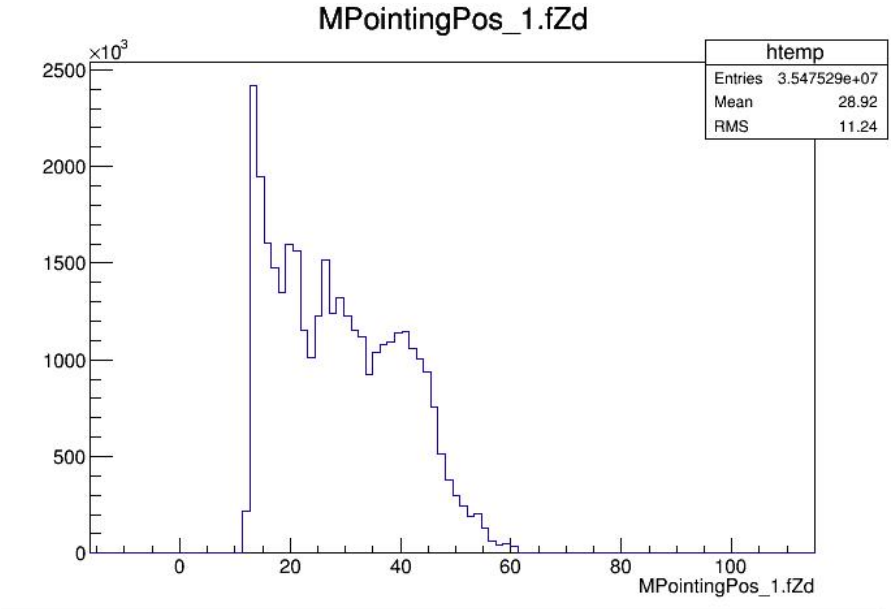

Figure 30: Plot of the zenith angles of Perseus_MA+NGC1275.

5.1 Description of the signal

VHE gamma-rays, coming from the possible decay of DM particles in Perseus galaxy cluster, travel almost undisturbed through the Universe and reach the Earth's atmosphere. When they start actively to interact with the electrostatic field of the atmospheric nuclei, each interaction between a VHE photon and a virtual photon of the electrostatic field generates an e^+, e^- couple that, subsequently, radiates photons through bremsstrahlung. This last radiation produces other e^+, e^- couples and so on, giving life to an EM shower, which process of multiplication of the number of e^+, e^- terminates when the kinetic energy of the electron/positron $E < E_C$, where E_C is a critical energy, which is ~ 86 MeV in the atmosphere. At this energy, energy loss through ionization starts to dominate. The particles produced during the EM shower travel at a velocity greater than that of light in the medium, the Earth's atmosphere, and therefore emit Cherenkov radiation, fundamental to allow the detection of the showers through IACTs, that base on this effect their working principle. MAGIC telescopes are focused at a distance of 10 km a.s.l., because this is the altitude at which the showers development occur. Thus, the Cherenkov light, coming from the EM shower, has a density on the ground proportional to the energy of the gamma-ray that has initiated the shower, and create a circular pool of light around the telescopes of ~ 250 m of diameter, if the light comes perpendicular to the Earth's surface, and considering that the Cherenkov angle of emission is about 1 deg (see Fig.31).

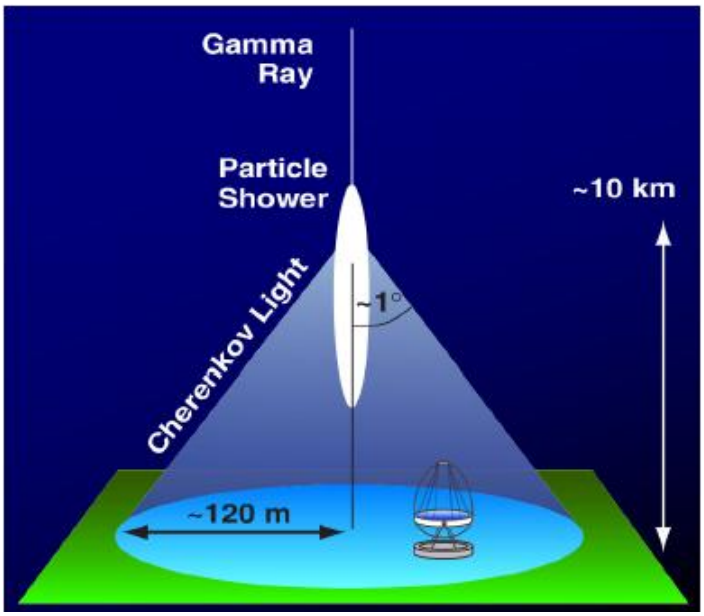

Figure 31: Pool of Cherenkov light. Credits: [30].

When looking for the extension of this light pool, then one has to take in consideration also the zenith angle at which one is observing. For low zenith angles, as the shower is almost perpendicular to the ground, the pool is smaller, but has an higher density of

photons for a given energy, while at high zenith angles the shower is more distant, the light pool is larger and the photon density is lower. In this last case, for high energy gamma-rays the A_{eff} (effective area) is larger. This last one is the area that must be used to calculate the physical properties of the sources in the sky and it is defined as

$$A_{eff} = \int P(x, y, E) dx dy$$

where$P(x, y, E)$ is the probability of triggering an event given its position in the camera (x, y) and its energy (E). For IACTs $A_{eff} \sim 10^4$ m^2 and its value becomes higher with the increasing of the energy.

5.2 Signal Reconstruction

When the Cherenkov light arrive to the camera, it is measured as a peak of charge (in photoelectrons) in a certain region of the camera and at a certain arrival time , followed by possible ringings. As first step of the reconstruction of the signal, from its waveform the baseline has to be subtracted, which is estimated through pedestal events, i.e events with random trigger that do not have any pulses inside. Successively, to detect the signal, the integration window has to be moved to a position in which the largest peak is found. In particular, the integration is done on 6 times slices (3 ns) searching in the whole window of 60 times slices. Then, now we have a signal for each pixel in a given event in units of integrated readout counts, but we want it in number of photoelectrons (phes). To convert one unit of measurement into the other, the F-factor method, that is based on the light pulses emitted by the calibration boxes, is used. Taking into account that

$$N = F^2 \frac{\mu^2}{RMS^2_{signal} - RMS^2_{pedestal}}$$

where the number of phes N for each event is expressed as function of the correction factor F^2 for non-Poissonian response of the PMTs -in general, it is assumed the Poisson statistic that lead to write the fluctuations of the signal as $RMS = \sqrt{N}/C$, with C number of phes for a readout count-, of the RMS for the signal and the pedestal events and of the number of counts μ for each event, the number of phes for each readout count results to be

$$C = \frac{N}{\mu}.$$

Then, as with this method we can convert the number of counts in number of phes, we can finally measure the signal as number of phes. Since PMTs differ from one another in the camera, even if the High Voltage (HV) is adjusted to have an homogeneous signal (flatfielding procedure), the illumination of all the camera shows different C for each pixel. Thus, in order to have the same signal all over the camera, the solution is not calibrate to real phes, but to equivalent ones as

$$C_{pixel} = \frac{N_{cameraaverage}}{\mu_{pixels}}.$$

In conclusion, we have now the signal expressed in numbers of photoelectrons, but now we need to know its arrival time and its position in the camera. As far as the arrival time concerns, it is defined as

$$t_{arrival} = \frac{\sum i s_i}{\sum s_i}$$

where i is the time slice number and s_i is the signal in slice i. The sum is performed over the slices the width of the integration window. Since there are discrepancies of the arrival times of the PMTs signals for a synchronous light pulse that illuminates all the camera, because of physical and technical limits, the solution is to calculate the mean arrival time in calibration pulse and subtract it from $t_{arrival}$.
After these procedures, one needs to clean the image from spurious events, specially because of lights related only to fluctuations of the Night Sky Background (NSB) or electronic noise, keeping in mind to cut signals up to a certain threshold -that has to be low enough to take low energy signals but at the same time it has to reduce maximally the noise. Different algorithms have been created for this purpose, and the one used is based on the number of photoelectrons of each pixel, taking into consideration if the peak is located in the core of the camera or in the boundary, and on the arrival time of the measured signal. The charge Q of the core has to be at leastQ $\{\text{core}\} = 6\,\text{phes}$ per pixel, while the one of the boundary has to be at least Q $\{\text{core}\} = 3.5\,\text{phes}$; peaks with charges lower than these are rejected. Moreover, selected pixels are marked as belonging to the core region if at least one direct neighbour had been selected in a previous step. Pixels of the core area with arrival times bigger than 4.5 ns with respect to the mean arrival times of the core pixels are rejected. This cut is used also for islands of boundary pixels, but with a range of time of 1.5 ns. Isolate pixels, that do not belong to the core or the boundary region, are rejected too. An example of how the image cleaning behaves on the camera pixels is shown in Fig.32.

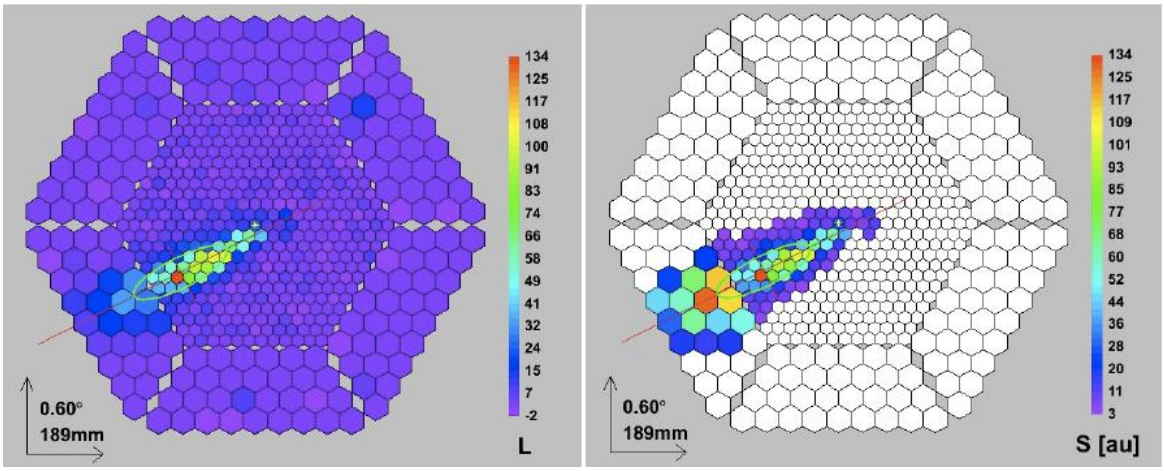

Figure 32: Recorded event on the camer before (left) and after the image cleaning. Credits: [30].

At this point, we have a physical signal for each Cherenkov photon that is fully reconstructed. Now, we can have a view of the whole event of the shower, that seems like an ellipse, by assigning to it the image parameters, i.e. precisely the ones that are related to the image of the shower in the camera. After this step we have now the basic set of information for the analysis, because of the fact that the Hillas parameters can be connected to physical parameters of the primary gamma-ray (energy, direction, arrival time).

5.3 Data Reconstruction

5.3.1 Image Parameters

In this section I will give a brief description of the most important Hillas parameters, i.e. the image parameters, named in this way because of the fact that the first ones were introduced by him in 1985. To better understand some of them, Fig.33 is shown.

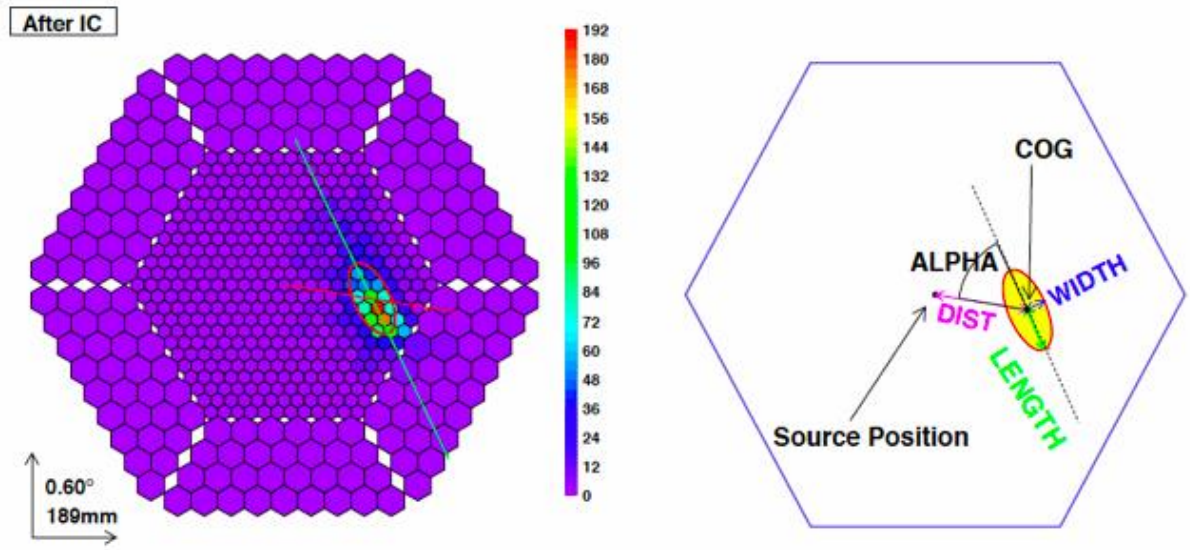

Figure 33: Sketch of an event, on the left, and its description in term of some image parameters, on the right. Credits: [14].

Size It is the global number of phes of an event and, in first approximation and for fixed values of the impact parameter and Zenith angle, it is proportional to the primary particle energy.

CoG The Center of Gravity of the image consists of a pair of values (^X, ^Y) that determine the position in the camera of the weighted mean signal along the X and Y axis respectively.

Width This is the half width of the minor axis of the shower ellipse and, as it is correlated to the transverse development of the shower, it is an important parameter for the discrimination between γ-initiated showers and hadronic showers. In fact, the transverse development of the latter is larger than that of the former.

Length It consists on the half length of the major axis of the shower ellipse. Since it is correlated to the longitudinal development of the shower that is larger for hadronic showers than for γ-initiated ones, as in the previous case, it is important for their discrimination.

Conc-n This is the fraction of phes contained in the n brightest pixels, that are the ones of the core of the shower. Also the Conc-n parameter can be helpful for the γ/hadron separation, since for γ-ray induced showers this region ought to be very compact.

Leakage Parameter used also for the calculation of the J-factor, as one can see in the next paragraph, that represents a fraction of signal distributed in the outermost camera ring with respect to the total size of the image. With it one can reject images that cannot be reconstructed correctly, as it estimates the fractions of signals loss because too large impact parameters.

M3long It is the third longitudinal momentum of the image along the major axis of the ellipse and measures the asimmetry of the signal along this axis. For this reason it is used to determine the head-tail discrimination of the shower. In fact, the head of a shower is supposed to be more charge concentrated than the tail.

Number-of-Islands As the name tells, it is the number of distinct islands in the shower image and, consequently, it tells us the fragmentation of the shower. Also this parameter allows the discrimination of the hadronic showers, more fragmented, from γ-induced showers.

These following two parameters, in particular, are related to the wobble mode of the observation, and are:

Alpha Angle between the major axis of the ellipse and the direction from the image CoG to the reference point, as one can see in Fig.30. It is the best parameter to distinguish hadronic showers from γ-initiated showers, since the latter point directly to the center of the camera and so they are characterized by small Alpha angles, on the contrary of hadronic showers. These have a rather flat Alpha, as their distribution in the camera is isotropic.

Dist It is the distance of the image CoG to the reference point in the camera.

Having defined all these parameters, we can now go on describing what one does usually to reconstruct data, as one can found the files where the image parameters are defined, named Star, in the MAGIC database. In fact, they are generated by the On Site Analysis (OSA).

5.3.2 Stereo Reconstruction and first selection of the data

The so-called Superstar files are obtained from the merging of two Star files, one for each telescope and concerning the same data taking time. Then, during this step, it is performed the stereoscopic reconstruction of the shower parameters. Let's have a look now on what happens during this reconstruction.

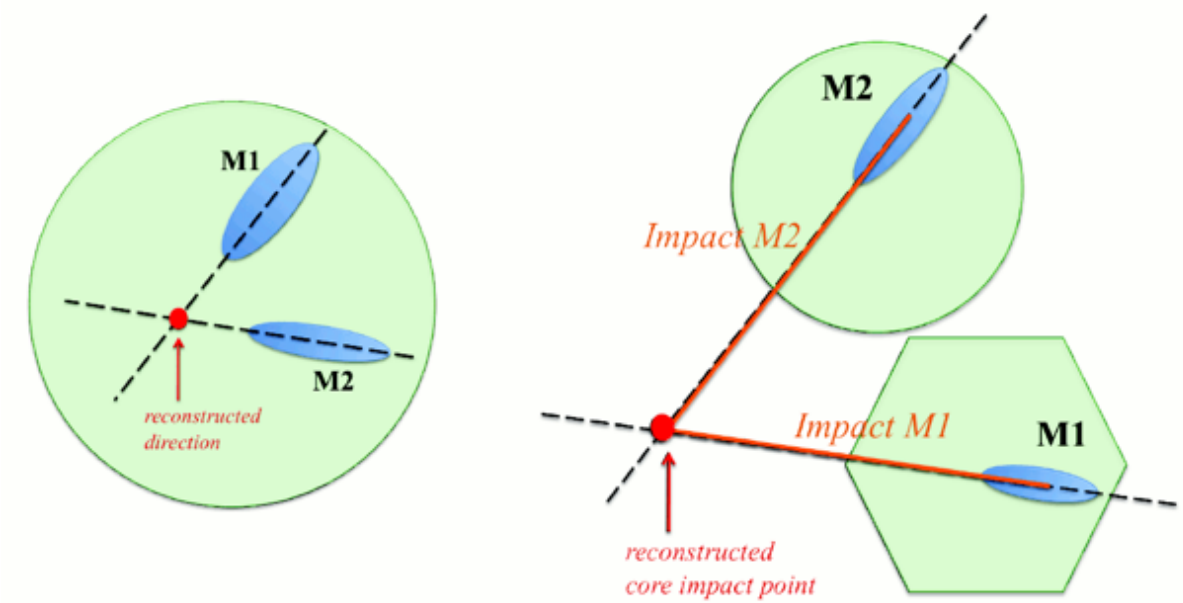

Figure 34: Particular of the reconstruction shower direction and of the core impact point of the shower. Credits: [15].

As one can see in Fig. 34, two of the parameters obtained during the stereo reconstruction are the incident direction in the sky of the primary γ-ray and the shower core impact on the ground. The former comes out from the intersection of the directions of the shower axes seen by each telescope. The latter is the intersection between the projection on the ground of the two plans that contain the shower axis and the telescopes positions. Both these parameters can be reconstructed in the correct way only if the angles between the two images axes are large enough. The impact parameter is then defined by the distance between the shower axis and the telescope position. The other parameter reconstructed is the height of the shower max, that is the altitude that minimize the distances between the shower axis and the two lines connecting the telescope position and the direction of the image centroid.
However, the calculation of these parameters is improved with the DISP method, i.e. a method based on the source position -this is the reason why it is called DISP, Distance between the Image centroid and the Source Position. If the reconstructed direction of the shower, taking in consideration only one telescope, is at a large distance from the reconstructed direction of the other telescope, this event is rejected. Consequently, this fact is used to discriminate between hadronic and γ-induced showers, as the former are more likely wrongly reconstructed and then rejected.
Let's have a look now on the samples of data used.

NGC1275

2013/09/13-2013/10/04-2013/10/09-2013/10/13-2013/10/31
2013/11/01-2013/11/02-2013/11/05-2013/12/31-2014/01/02
2014/02/23

Perseus_MA

2013/07/30-2013/07/31-2013/08/01-2013/08/02-2013/08/03
2013/08/07-2013/08/09-2013/08/11-2013/08/28-2013/08/30
2013/08/31-2013/09/02-2013/09/05-2013/09/07-2013/09/13
2013/09/15-2013/09/17-2013/11/22-2013/11/24-2013/11/25
2013/11/26-2013/11/27-2013/12/07-2013/12/08-2013/12/09
2014/01/06-2014/01/07-2014/02/02-2014/02/04-2014/02/05
2014/03/03-2014/03/04-2014/03/05-2014/03/09

The zenith angles covered by these samples are the ones in Fig. 35.

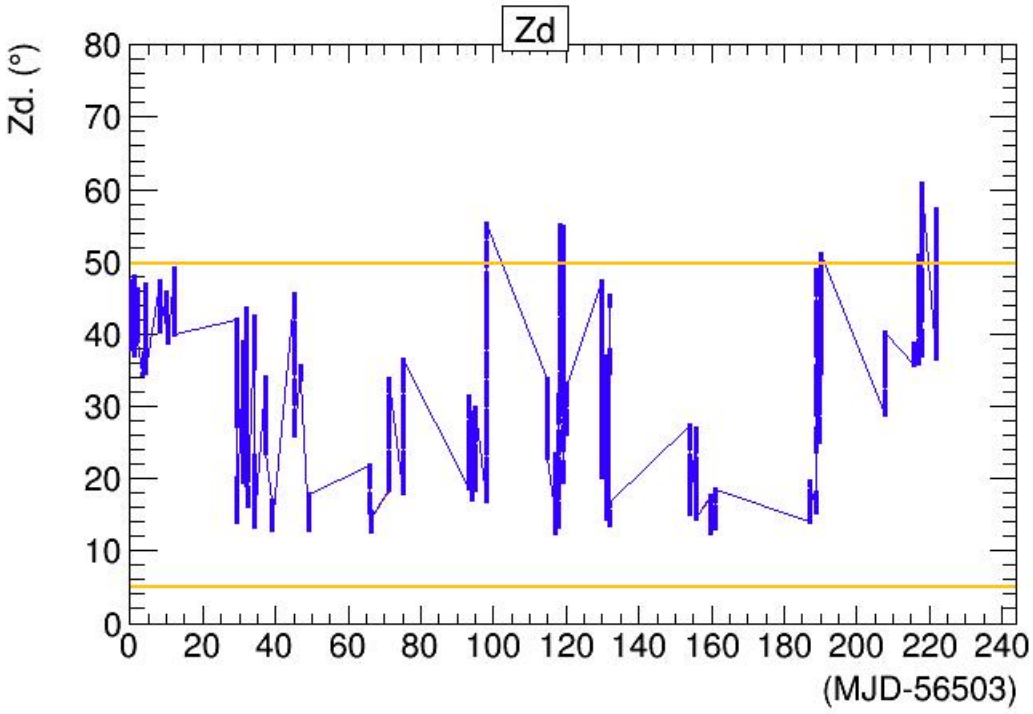

Figure 35: Zenith angle distribution with the cut lines showed in yellow.

The figure shows the distribution of the zenith angles in the period we considered for the analysis, where data with zenith angle above 50° have been rejected. MJD is the acronym of Modified Julian Date. This unit of measurement of time has its starting point at the midnight of the 17th of November 1858.
Now that we have our data, i.e. files containing parameterized events, we have to discriminate them, cutting out the hadronic showers and the background signals, in order to have, at the end, only signals that are marked to be γ-rays by the hadronness parameter, possible consequence of the decay of DM particles in Perseus galaxy cluster. The constraints used for the analysis are firstly based on the mean DC current in the telescopes: it has to be lower than $2\,\mu$A to reject all moon light and twilight observations, keeping only observations taken during dark nights, and also to rejects the noise events that had lighted up the camera. The maximum value set for the DC is the limit used for standard analysis, while higher values are used for non-standard ones, that need different image cleanings from the one used. Another threshold for the data is given by the transmission of the signal in the atmosphere, in particular the limit had been set at 55% of transmission at 9 km a.s.l.

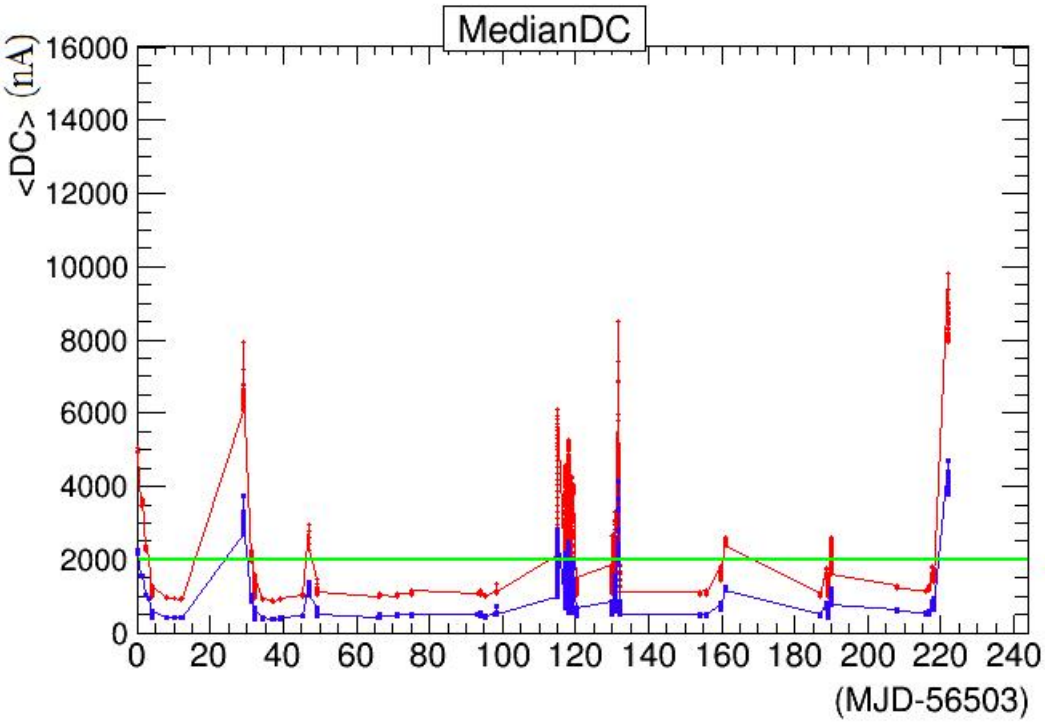

Figure 36: Distribution of the mean DC for MAGIC telescope 1 (M1) in red and for MAGIC telescope 2 (M2) in blue with the line of the cut showed in green.

As one can see in Fig.36, the DC current of M1 is higher than that of M2 and this is due to the different PMTs used in the two cameras, as it is explained in §3.1.3. The transmission in the atmosphere is showed in the following image. Both the two cuts

had been done on time slices, of the order of 2 minutes, instead of runs, in order to keep the maximum number of data. This means that we consider for each day a period of time that goes from the beginning to the end of the observations. Then, we divide it in slices of 2 minutes each and we determine, through the constraints we have defined, those to cut. Moreover, during this step of the analysis, the averages of the parameters are done too.

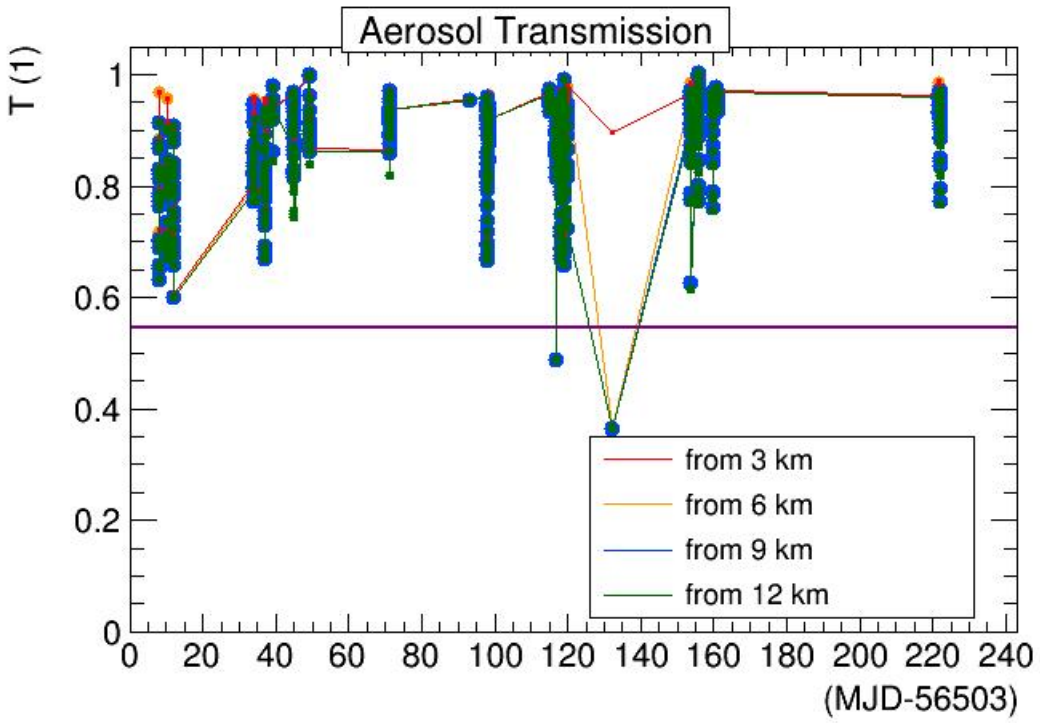

Figure 37: Aerosol transmission at different altitudes (3 km a.s.l.,6 km a.s.l.,9 km a.s.l.,12 km a.s.l.) with the line of the cut showed in violet.

Among all these data also events coming from accidental triggers, e.g. background light, electronic noise etc., and from muons, that hit near the telescopes at ultra-relativistic velocities and generate rings or section of rings on the cameras, are present, together with the ones we are interested in, that are the extensive air showers (EAS). This last sample can be divided into two parts: the hadronic showers and the γ-induced ones. After having rejected the most of the first two classes of signals, what remains to do is to divide the EAS observed and to concentrate only on γ-induced showers. The purpose is achieved by assigning a parameter, called hadronness, to each event that goes from 0, for images produced by γ-rays, to 1, and it describes the hadronic behavior of the data taken basing itself on the image parameters distributions, as said in the first part of the paragraph. The haddronness is defined by decisional trees, called Random Forests (RFs), that are algorithms trained with events of known nature: Monte Carlo[29] (MC)

[29]A problem solving technique that is used to approximate the probability of certain outcomes by

simulated γ-ray events and hadron events extracted from an "off source", i.e. a source in which is known, from previous analysis, that γ-ray events are not present.
An essential aspect to keep in consideration here is that the reason for using MCs and off sources is the fact that we don't have a system that can create Cherenkov light coming from γ-induced events, that is what we need to calibrate our instruments.

5.3.3 Monte Carlo Simulations

The simulations adopted for the analysis reproduce γ-induced signals coming from a generic extended source, as Perseus is extended, and take into account the configurations of the telescopes. They are divided into subsamples with different zenith ranges (05°-35°, 35°-50°, 50°-65° etc.) and we consider only the ones covering the zenith angles of the source, so 05°-35° and 35°-50°. The samples having the same zenith angle range splitted into two files: one with the 30% of the events (the test) and the other with the 70% of the events (the train). The train sample has been used to create the RFs together with the off source samples, of which I will talk in the next sub-paragraph. The reason that led to do this is the fact that the off source is mostly dominated by hadronic events, while the MCs are only γ-induced events. The test part, differently, is used as sample of data to be analyzed and it is fundamental to evaluate the Instrument Response Function[30] (IRF) of the telescopes. During this process, events simulated at a distance from the center of the simulated source lower than 0.1° and higher than 0.7° are rejected. In fact, as the observations have been done in wobble mode at a distance of 0.4° from the center and the source has an extension of 0.3°, one considers only simulated signals coming from the region between 0.4°-0.3° and 0.4°+0.3°.

5.3.4 Off Source

As off source I decided to use a combination of two sources: B1957+20 and BZBJ0123+342. The reason for this choice is due to the fact that the off source has to be dominated by hadronic events -it has to be a source already observed and in which no signal excesses have been measured- and in the same zenith angle distribution of Perseus observations, in order to avoid artifacts in the training. The data samples used are the following: BZBJ0123+342 covers the zenith angles from $\sim 5°$ to $\sim 40°$ and B1957+20 from $\sim 40°$ to $\sim 50°$, for a total time of observation of ~ 10.6 h.

BZBJ0123+342

2013/10/01 (runs 5029661-5029662-5029663) - 2013/10/08 (runs 5029892 5029893) - 2013/10/09 (runs 5029931-5029932-5029933-5029934-5029935

running multiple trial runs, the simulations, using random variables.

[30] It is the mapping between the photon flux that hits the instrument and the detected events. This quantity does not depend only on the hardware, but also on the assignment of the parameters during the analysis.

5029936-5029937-5029938-5029939-5029940-5029941-5029942-5029943
5029944-5029945-5029946-5029947)

B1957+20

2013/08/31 (runs 5028875-5028876-5028877) - 2013/09/04 (runs 50289031
50289032-50289033) - 2013/09/13 (runs 5029315- 5029316-5029317) -
2013/09/14 (runs 5029359-5029360-5029361)

The cuts used to check the data are the same used for Perseus ($5° \leq$ zd $\leq 50°$, transmission in the atmosphere at 9 km a.s.l.≥ 0.55 and mean DC $\leq 2000\mu$A), as you can see in the following figures.

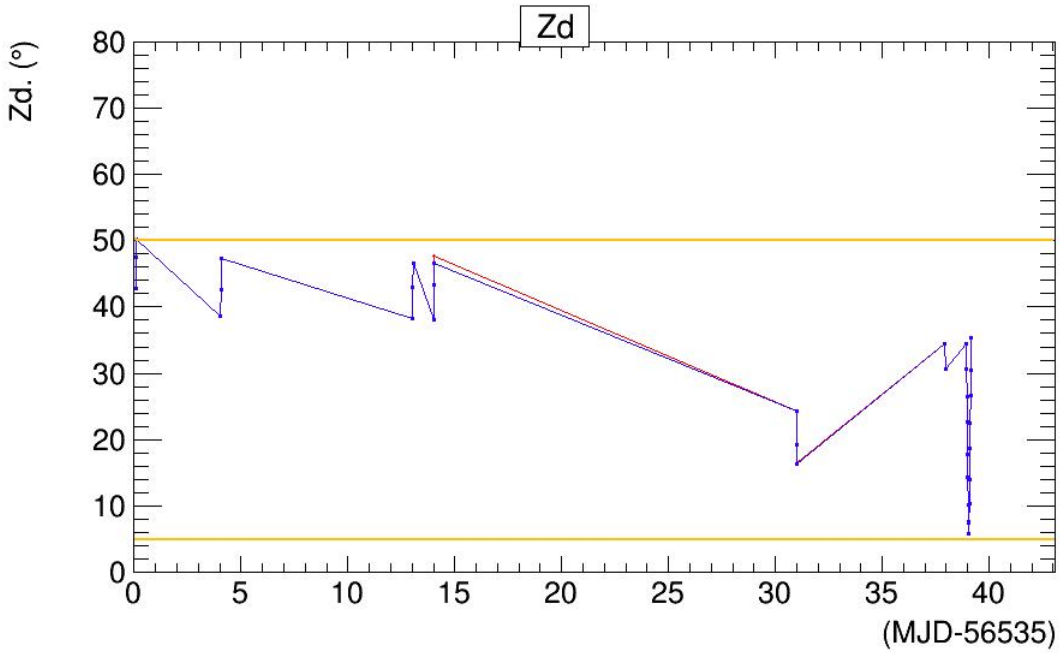

Figure 38: Zenith angle distribution with the cut lines showed in yellow.

Looking at the figure, the zenith distribution showed is just inside the range, as I wanted to have. The red line is due to the covering of the same zenith angles by the two sources.

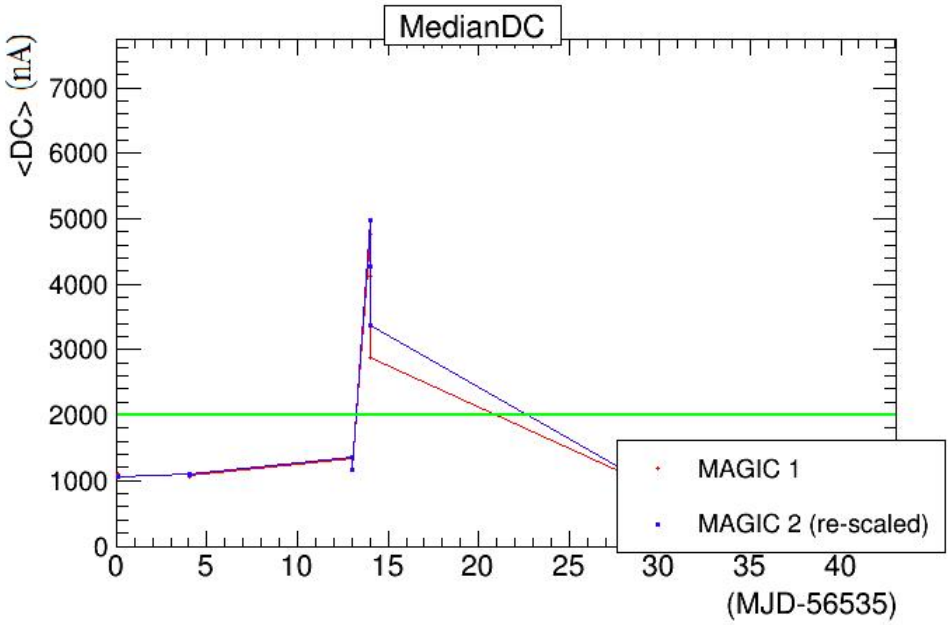

Figure 39: Distribution of the mean DC for MAGIC telescope 1 (M1) in red and for MAGIC telescope 2 (M2) in blue with the line of the cut showed in green.

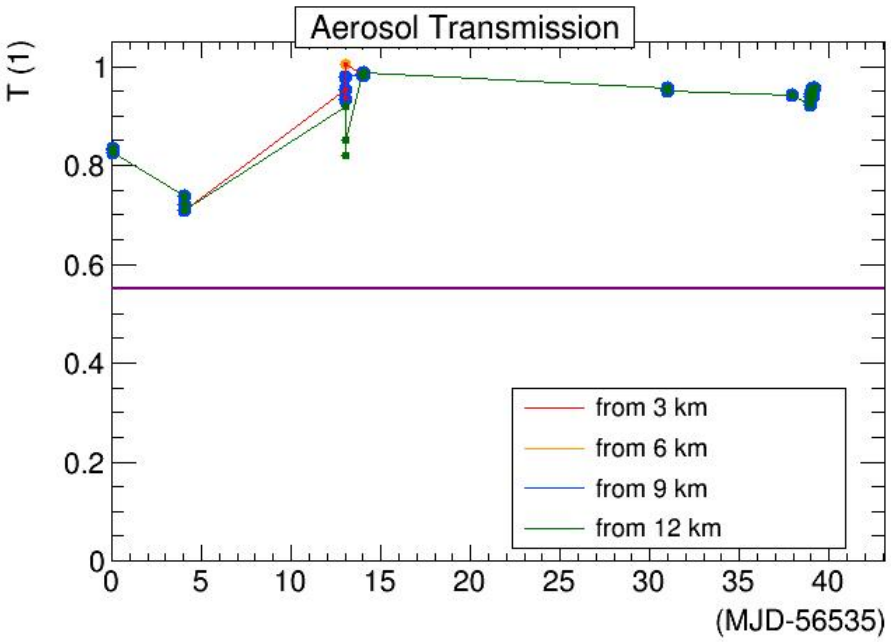

Figure 40: Aerosol transmission at different altitudes (3 km a.s.l.,6 km a.s.l.,9 km a.s.l.,12 km a.s.l.) with the line of the cut showed in violet.

Then, once these RFs are created they are applied to the data to assign the hadronness parameter. The result is the following.

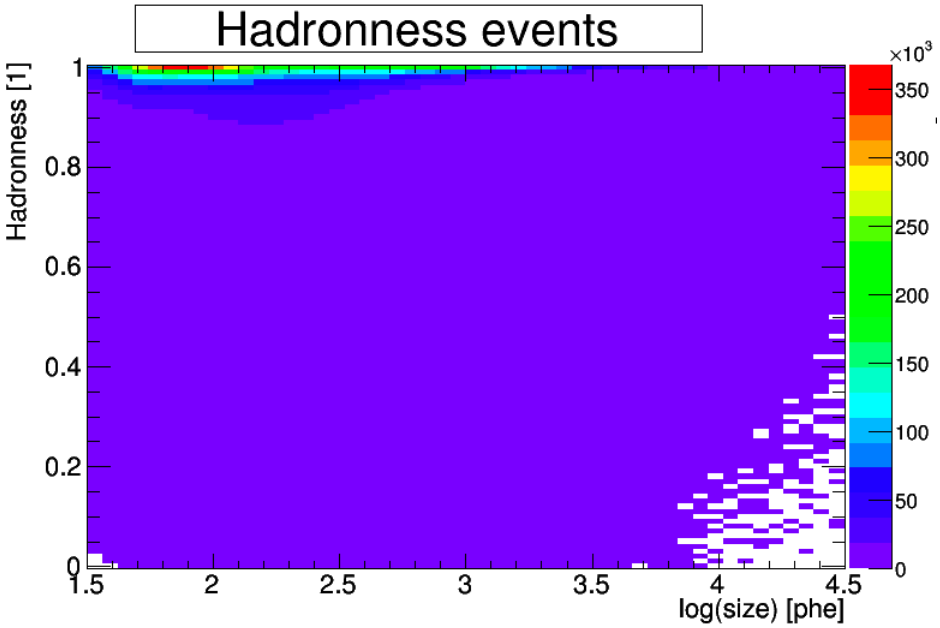

Figure 41: Hadronness parameters distribution.

Moreover, also energy tables and DISP parameters are created using the off source and the MCs and are used to estimate the energy and the position of each event respectively. However, what has to be clear here is that we are working only with raw data until now, because no physical quantities have been taken into consideration yet, only geometrically reconstructed parameters have been used.
To prove the performance of the analysis, the same cuts and processes applied on Perseus have been used for the Crab Nebula. It is a standard candle since decades, as it is very well known and it is observed regularly by the MAGIC telescopes. The sample of data used, covering the zenith range between and for a total time of observation of $\sim$ 6.9 h, is the following:

CrabNebula

2014/02/07 (runs 05032941-05032942) - 2014/02/22 (runs 05033097-05033098-05033099)

2014/02/25 (runs 05033190-05033191-05033192-05033193) - 2014/02/26 (runs 05033221

05033226-05033230-05033231-05033232) - 2014/02/27 (runs 05033276-05033277

05033280-05033281-05033282-05033283-05033286-05033287-05033290-05033293

05033294)

The zenith angle distribution is the one in Fig.42.

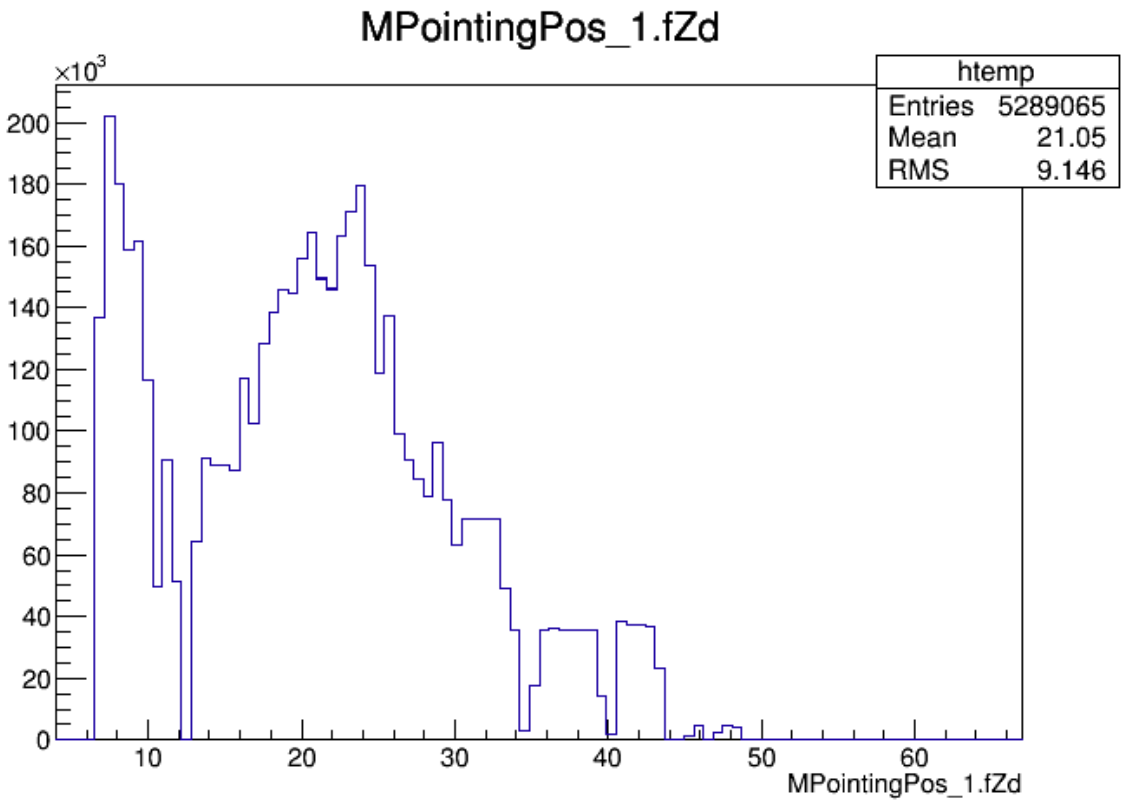

Figure 42: Crab Nebula zenith angle distribution.

With the information reconstructed on the events we can now distinguish between hadron and γ-induced showers and so we can look at the possible excesses of γ-induced signals respect to the background.

6 LOWER LIMITS ON DM DECAY IN PERSEUS

6.1 Energy Reconstruction

Once recognized the γ-induced signals, one has to evaluate their energies. In MAGIC analysis this is done through the use of Look Up Tables (LUTs). These ones are based on MC simulations: the training sample of the MC is divided in bins, each representing one of the parameters for the energy reconstruction (size, impact parameter, height of the shower max, zenith angle, azimuth, position in the camera, etc.). Consequently, a multi-dimensional table that contains the mean energy and the RMS of the MC events belonging to each bin is built. The energy estimated for an event in Perseus is then stored in the table for the multi-parameters bin corresponding to that event. However, the precision of the energy reconstruction is limited by the fact that we can not have an infinite number of bins and parameters and so a minimum number of event, sufficient to provide a sensible mean value, has to be contained in each bin. Since the bin event population has to be homogeneous and the variation bin to bin relatively smooth, one has to choose wisely the used parameters and the binning. Thus, to simplify the table it is better to begin from a rough approximation of the energy, described as the size of a signal, and little by little correct it. The corrections applied concern: zenith angle corrections, leakage corrections and geomagnetic field corrections. The latter deflect slightly the electrons and positrons of the shower in opposite directions, spreading the full shower. This fact leads to a lower density of the light reaching the telescopes.
In this analysis we did not use the energy reconstruction only to know the energy of the singles γ-rays, but also to evaluate other parameters, like the effective area, the hadronness, etc., but we will see it in the next paragraph.

6.2 Full Likelihood Method

Looking at the plots if Fig.43-44, one can see that the region observed do not present extended excess, except for the point-like signal of NGC1275 in the center of the camera. In fact, we would mark an excess as a signal only if the significance Li&Ma[31] is $\geq 5\sigma$.θ^2 is defined as the square of the angular distance from the center of the source. The dotted vertical lines determine the region in which the excess is expected, so where one has to search for the signal.

[31] Significance based on the experimental parameters.

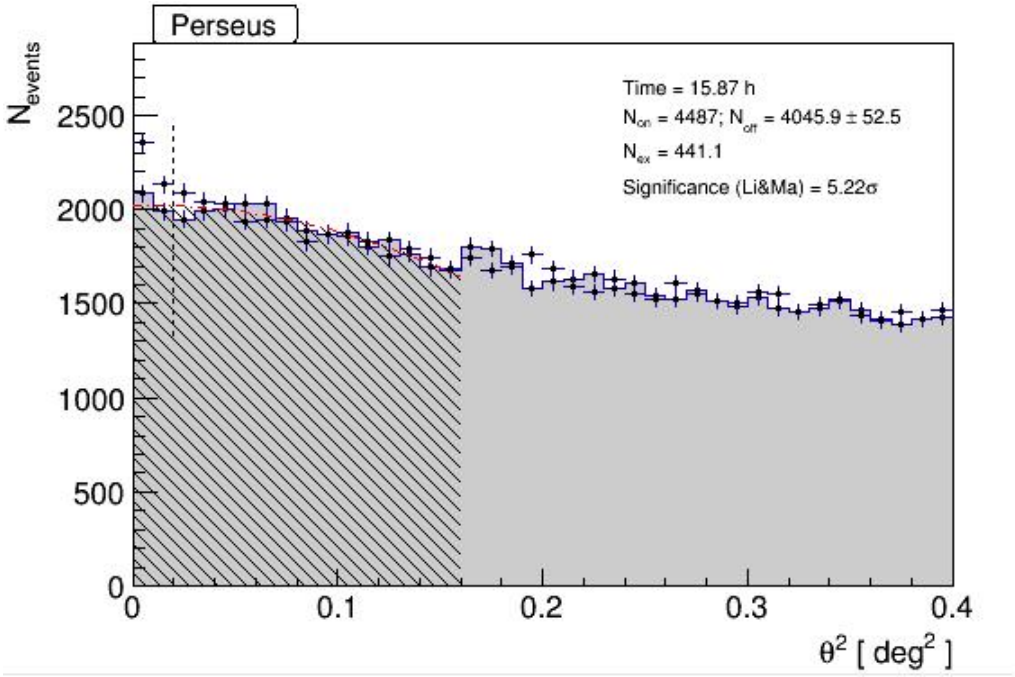

Figure 43: Theta-square plots of Perseus galaxy cluster in the low energy range.

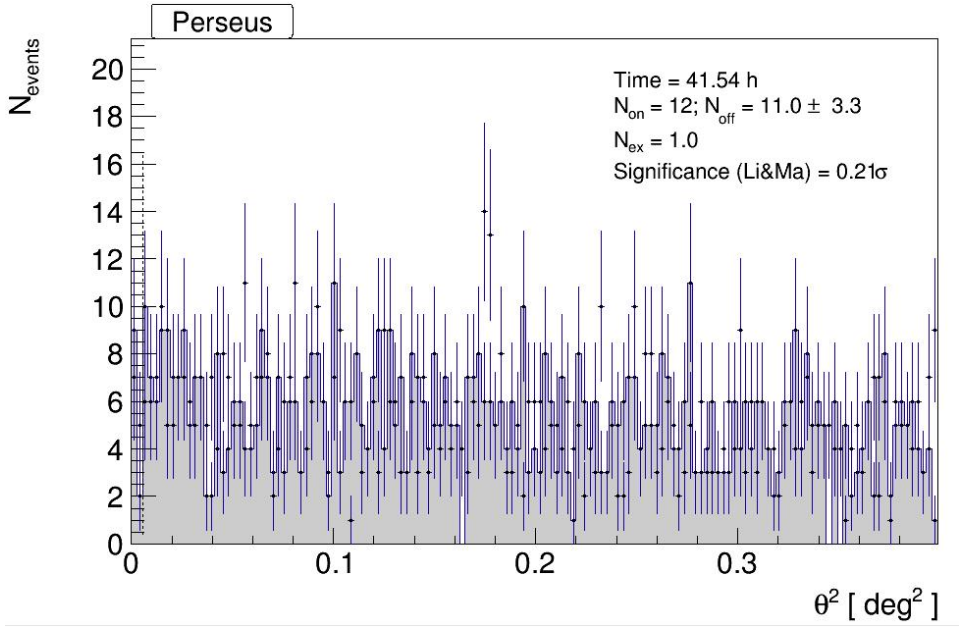

Figure 44: Theta-square plots of Perseus galaxy cluster in the high energy range.

In both plots, at low energies and at high energies , only the signal of the AGN of the galaxy NGC1275 is visible at low energies, but, except for that, no extended signal are present. Then, after having assigned the parameters to all the data and not having

seen any excess in the plot, it follows that we need a method to estimate at least an upper limit on the flux of decaying DM particles. The lower limit on the mean lifetime of those decaying particles will follow directly using the formula of the flux written in chapter 4, but we will see in details this procedure in the next lines. To look for the upper limit on the flux, the Full Likelihood method, based on an a priori knowledge of the expected spectral shape, had been used. This is a statistical method based on a function, the likelihood, that calculates the probability to obtain a certain θ parameter given the values of the data x, $L(\theta; x)$.
In particular, what we aim to obtain here is the maximum value of the flux besides which the probability to find γ-induced signals, given by decaying DM particles, is lower than 5%, i.e. we have the probability of the null hypothesis[32] for the 95% of the cases above the values we calculate for the upper limit. What one does, then, is to minimize the likelihood ratio λ, that is the ratio between the likelihood function and the same function in which the values of the parameters are set in order to minimize it. But let's see the analysis in details. The likelihood function used for this method is not the common one used for the Rolke method [13],usual for standard MAGIC analysis, but a different one, that increases the sensitivity for gamma-ray searches, given by

$$L(s,b|E_1,...,E_{N_{ON}},E_{N_{ON}+1},...,E_{N_{ON}+N_{OFF}}) = \frac{(s+b/\tau)^{N_{ON}}}{N_{ON}!}e^{-(s+b/\tau)} \times \frac{b^{N_{OFF}}}{N_{OFF}!}e^{-b} \times$$

$$\times \prod_{i=1}^{N_{ON}} f(E_i|s,b) \times \prod_{i=1}^{N_{OFF}} g(E_i,b)$$

where s is the estimated number of gamma-ray events in the ON region and b is the estimated number of background events in the ON region (these two are the parameters of the likelihood function), τ is the normalization between ON and OFF exposures, N_{ON} is the number of events measured in the ON region, N_{OFF} is the number of events measured in the OFF region, f and g are the PDF of the reconstructed energy in ON and OFF events. Comparing this method to the other one used in MAGIC collaboration (the Rolke method), the fundamental aspect is the fact that here the significance is not yet calculated averaging on the whole area of the θ^2 cut, the region delimited by the dotted line in Fig.38-39, but comparing the signal to the background for each photon, keeping in consideration the spectral profile. The fact that this likelihood is based on the energies of single photons can be noticed by the products in the last part of the formula, that differs from the usual likelihood formula. The fundamental inputs for this method come from the estimation of the effective area A_{eff}, of the energy resolution E_{RES} and of the energy bias E_{BIAS}. These three quantities have been obtained basically from MC simulations and, obviously, from the data samples. In particular, the A_{eff} is calculated using the formula

$$A_{eff} = A \times \frac{N_{\gamma,final}}{N_{\gamma,simulated}}$$

[32]The probability that an event does not occur.

where A is the area within which the MC gamma-ray events have been generated with an homogeneous distribution and that is orthogonal to the gamma-rays direction, $N_{\gamma,simulated}$ is the total number of the simulated gamma-rays, also those not triggering the telescopes, and $N_{\gamma,final}$ is the final number of gamma-rays after the analysis cuts. The effective area depends on different parameters: the true energy[33] of a gamma-ray, the pointing direction of the telescopes (zenith and azimuth angles) and the direction of the gamma-rays within the FoV of the telescopes. All these quantities can be obtained from MCs, except for the location of the source in the FoV, that has to be selected looking at the real data in order to have the MCs with the right offset angle of the wobble and the right amount of time spent by the source in each part of the camera.
Going into details in the Full Likelihood Method to calculate the flux upper limit, we can rewrite the last two products of the formula as

$$f(E|s,b) = \int_0^\infty \frac{d\Phi_b}{dE'} R_b(E;E')dE' + \int_0^\infty \frac{d\Phi_s(s,b)}{dE'} R_s(E;E')dE'$$

and

$$g(E,b) = \tau \int_0^\infty \frac{d\Phi_b}{dE'} R_b(E;E')dE'$$

where E' is the true energy, $\frac{d\Phi_{b,s}}{dE'}$ are the differential fluxes that depends on the parameters b, s, and on the spectral distribution of DM in the region observed, and $R_{b,s}$ are the IRFs of the telescopes, that depends on A_{eff}, E_{RES} and E_{BIAS}. The upper limit on flux we are interested in is then obtained through the reversing of the above formula, defining a minimum value of the energy. For more details have a look at [2].

6.3 Lower Limit on DM lifetime

6.3.1 Usage of the Full Likelihood Method in Perseus

Reminding at the paragraph 4.1, the formula for the flux is given by

$$\frac{d\Phi_\gamma}{dE} = \frac{1}{4\pi m_{DM}\tau_{DM}} \frac{dN_\gamma}{dE} \times J(\Omega).$$

To obtain a lower limit on the mean lifetime of a DM particle τ_{DM} one has to reverse the expression in the following way, taking into account that now one has an upper limit on flux,

$$\tau_{DM,LL} = \frac{1}{4\pi m_{DM} \frac{d\Phi_{\gamma,UL}}{dE}} \frac{dN_\gamma}{dE} \times J(\Omega).$$

It is clear that what is useful to find out the DM lifetime, or, better, the lower limit for it, is to know the DM mass m_{DM}, the upper limit (UL) of the differential flux of

[33] Proper energy of a simulated gamma-ray.

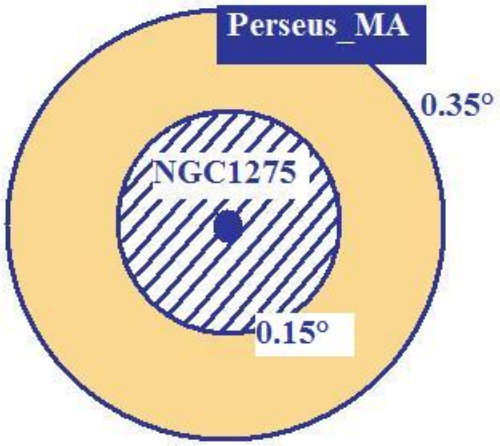

Figure 45: Ring of interest around the center of the source.

γ-rays coming from its decay, the produced number of photons in the decay $\frac{d\Phi_\gamma}{dE}$ and the J-factor. As far as the upper limit on flux concerns, it has been obtained thanks to the usage of the Full Likelihood Method, while the J-factor and the number of photons have been calculated. The calculus of these last factors has been restricted on a limited area of the source extension for two reasons: to look for the maximum ratio of the signal on the background and to exclude the emission area of NGC1275. The exclusion has been done only to cut out the signals coming from NGC1275, but the area will be considered for successive analysis. Looking at Fig. 45, one can observe the region of interest.
The cut at 0.15° has been applied due to extended emission of NGC1275 (the optimization of this cut will be at 0.20°, but this will be done in future works), while the cut at 0.35° has been done in order to maximize the Q-factor (see § 4.5). The number of photons for a given energy, then, have been obtained directly from the data reconstructed and taking in consideration the ring around the center of the source. The J-factor has been obtained as described in paragraph 4.5 and indeed taking into account the restriction on the area. Since the DM profile decreases with the distance from the center, as described by the NFW formula, a little amount of DM is present at 0.35°. For this reason one has to subtract this contamination and the values for the J-factor obtained are:

$$J(\theta_{min} = 0.15°; \theta_{max} = 0.25°) = 1.55673 \times 10^{18} [\mathrm{GeV\,cm^{-2}}]$$

$$J(\theta_{min} = 0.25°; \theta_{max} = 0.35°) = 1.33188 \times 10^{18} [\mathrm{GeV\,cm^{-2}}].$$

The last thing that we need for the calculus of the lower limit is the mass of DM. Surely, we don't know its value, but we can take into consideration a range of masses going from 10^2 GeV to $\sim$ 10 TeV to estimate the lower limits on DM particles lifetime. In

particular, we aim to find the limits for DM particles decaying with 100% branching ratio into $\tau^+\tau^-$ or $b\bar{b}$, as these two are the extreme limits of the decays into leptons and into hadrons respectively, because these are the particles with the higher masses of the two categories. The former have a continuous spectrum of gamma rays more harder (producing more high energy gamma rays) than the latter, that produces gammas at lower energies because of the hadronization of the quarks. The differences in the two spectra can be noticed in Fig.46, where different spectral energy distributions of different decay channels have been plotted defining DM masses of 500 GeV or 150 GeV.

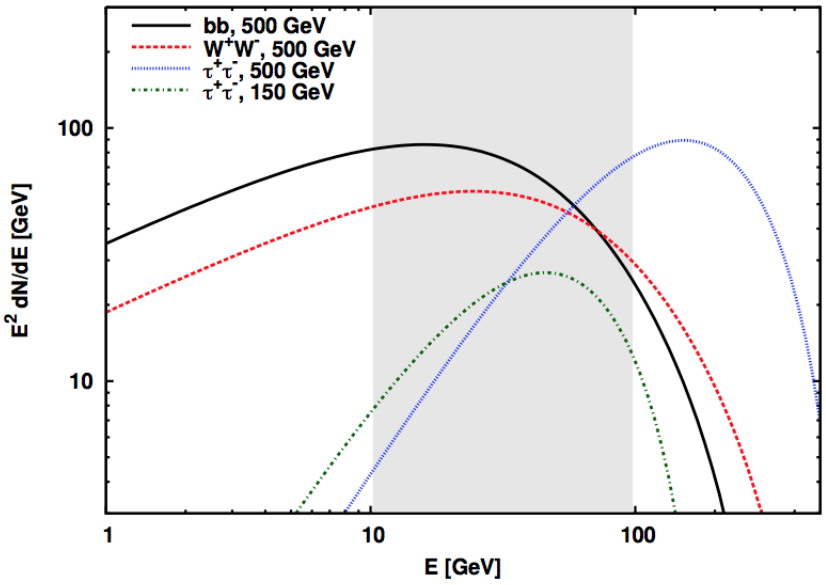

Figure 46: Spectral energy distributions of different decay channels. Credits: [Doro private comunication].

The possible theoretical models that gives us these decay products are the ones described in the next lines.

6.3.2 Dark Matter decay models

The theoretical models that describe DM decay, and that we consider here, are mainly based on the breaking of a symmetry and are divided into three groups, in consequence of the products after the cascade decay, that are: lepton, hadron+ lepton and hadron. In particular, the symmetry taken in consideration is the R-parity, that makes the DM particles stable if it is conserved. Talking about the R-parity violation (RPV), the particles that decay emitting radiation are:

Wino This particle is the supersymmetric particle of the W boson and the neutral wino $\tilde{W}_0$is the LSP that could be a possible candidate for DM with a mass

of a few hundred of GeV or around 3 TeV. Its decays are: $\tilde{W}_0 \to \nu e^- e^+$, $\tilde{W}_0 \to \overline{\nu} e^+ e^-$, $\tilde{W}_0 \to \nu_e \mu^- \mu^+$, $\tilde{W}_0 \to \overline{\nu}_e \mu^+ \mu^-$, $\tilde{W}_0 \to \nu_\mu e^- \mu^+$, $\tilde{W}_0 \to \overline{\nu}_\mu e^+ \mu^-$, and are possible only if the R-parity symmetry is violated. Among these decays, the IC photons are the only observable gamma rays because, otherwise, without the IC scattering, those photons would not have sufficient energy. Also the $\tau^\pm$ could be produced and are detectable through energetic gamma-rays directly.

Sneutrino This particle is the superpartner of the right-handed neutrino and the lightest one decays, in the RPV scenario, into: $\tilde{\nu}_R \to l^+ l^-$.

Gravitino If one consider the case of the R-parity conservation, the NLSP (next-LSP, i.e. the particle a little bit heavier than the LSP) is long-lived and may decay into gravitino (LSP) and other SM particles after the Big Bang Nucleosynthesis (BBN) started. On the contrary, in the RPV scenario, the decay occurs before the BBN and the gravitino produced could be a DM candidate. It is long-lived because of the suppression of its decay rate by the Planck mass and because of the small violation of the R-parity. The possible decays of this DM candidate are: $\tilde{g} \to \gamma\nu$, $\tilde{g} \to W^\pm l^\pm$, $\tilde{g} \to Z\nu$ and $\tilde{g} \to h\nu$. The decay into $\tilde{g} \to W^\pm l^\pm$ has the largest branching ratio and the products of this are high-energy electrons/positrons, gamma rays and protons/anti-protons (this last case studied specially for the excess of positron).

Axino Being the superpartner of the axion, even if it has a mass of $\mathcal{O}(10\,\mathrm{GeV})$ it can be sufficiently long-lived, i.e. with the lifetime necessary for the structure formation and that agrees with experimental results, to be considered a possible candidate for DM. Its decays are three-body processes and involve hadrons, they are $\tilde{a} \to udd$ and $\tilde{a} \to \bar{u}\bar{d}\bar{d}$. These quarks are then hadronized to produce mesons that decay into gamma rays or electrons/positrons (source of IC photons). Also the case of the decay into $b\bar{b}$ can be taken into consideration.

For more details about these DM candidates and the processes involved see [8, 26].

6.3.3 Perseus results

Having all the values to insert in the formula written above, the results obtained are shown by the curves present in the following figures.

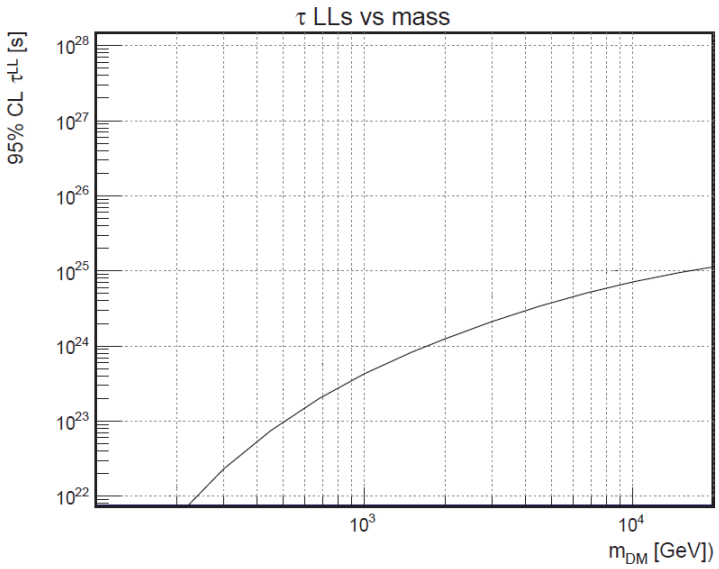

Figure 47: Curve of the lower limit of DM lifetime for $b\bar{b}$ decay channel in the range of mass between $\sim 10^2$ GeV and ~ 10 TeV.

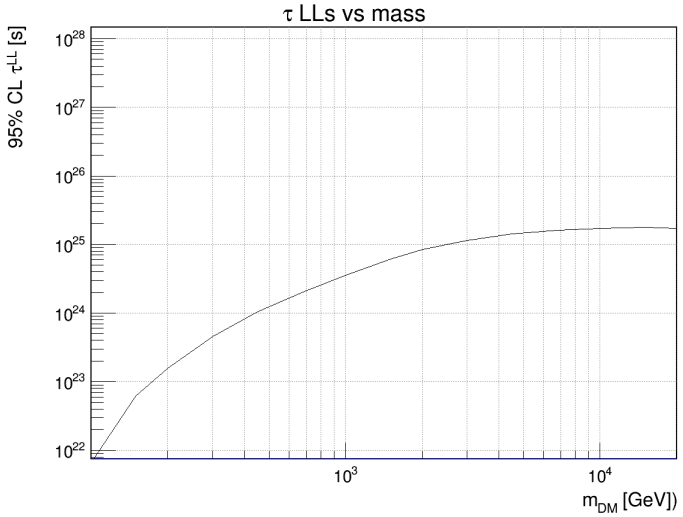

Figure 48: Curve of the lower limit of DM lifetime for $\tau^+\tau^-$decay channel in the range of mass between $\sim 10^2$ GeV and ~ 10 TeV.

7 CONCLUSIONS & OUTLOOK

The study of DM decay in Perseus galaxy cluster, right now, is only at the beginning of its life. The results obtained took into consideration a little part of the total amount of data availables. Nevertheless, the curves showed for the two decay channels give limits on DM lifetime a little bit stronger than those of previous analysis done by Fermi-LAT and HESS , that studied other cluster of galaxies (Fig.48).

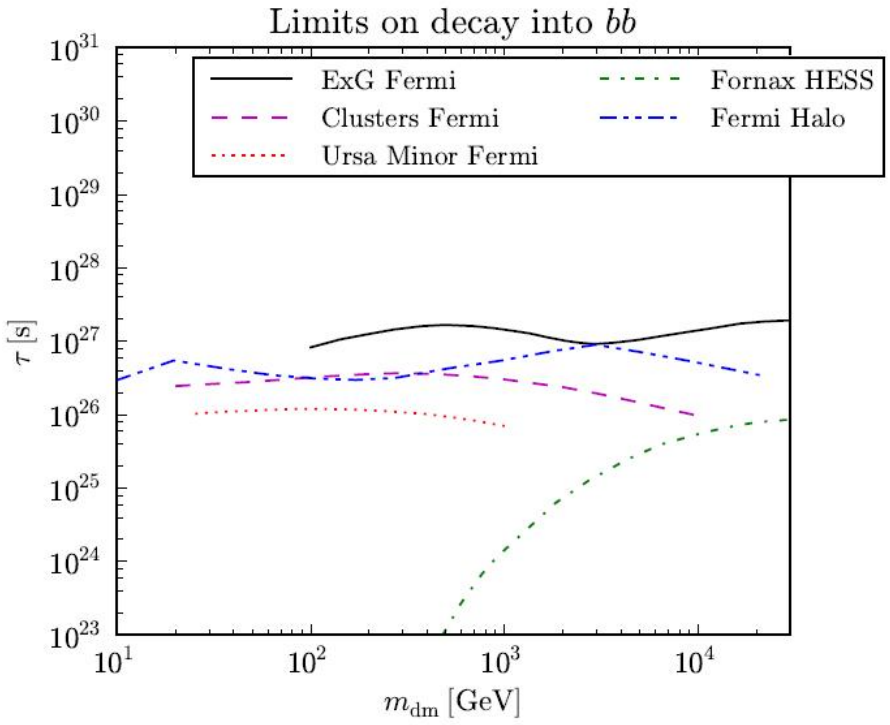

Figure 49: Limits on decay into $b\bar{b}$ obtained by Fermi-LAT and HESS analysis on different sources. Credits: [26].

Extrapolating the curves with the total amount time of observations in Perseus ($\sim$ 300 hours) the results are the following.

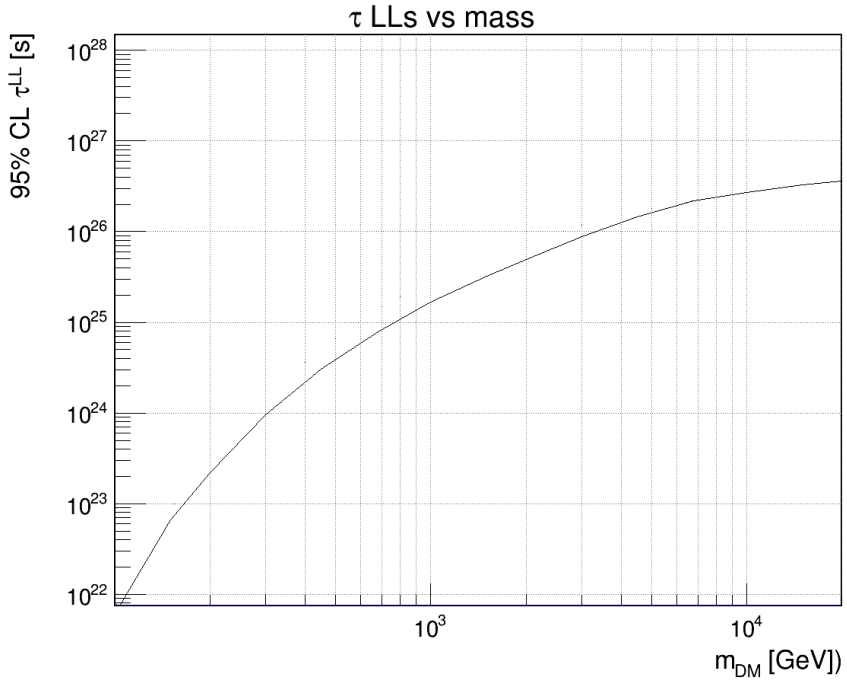

Figure 50: Extrapolation of the lower limit on DM lifetime for $b\bar{b}$ channel.

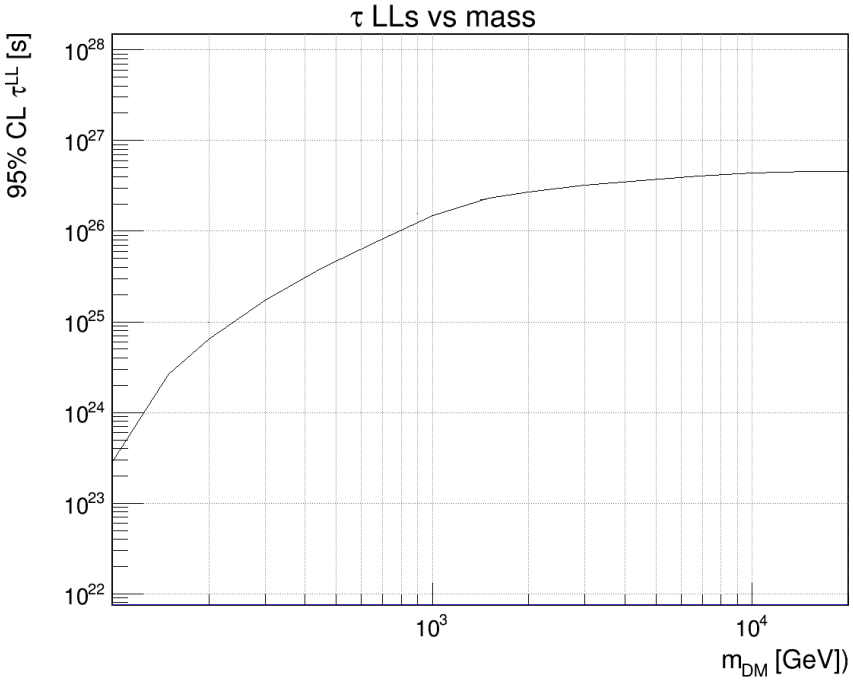

Figure 51: Extrapolation of the lower limit on DM lifetime for $\tau^+\tau^-$ channel.

As one can notice looking at the plots is that the limits are worst than those obtained

with a restricted amount of data. In fact these are only preliminary studies, much more work have to be done. At a later time, the internal area will be included in the calculations and strongest cuts, as the one in hadronnes, will be applyed. Moreover, Perseus_MA data sample will be added to our data in order to obtain a lower limit on DM lifetime with more statistics.
With future works, however, different sources will be analyzed, maybe using different detectors, as for example CTA, and hopefully better results will be reached.

References

[1] R. Adam et al. Planck 2015 results. I. Overview of products and scientific results. 2015.

[2] J. Aleksic, J. Rico, and M. Martinez. Optimized analysis method for indirect dark matter searches with Imaging Air Cherenkov Telescopes. *JCAP*, 1210:032, 2012. doi: 10.1088/1475-7516/2012/10/032.

[3] J. Aleksic, S. Ansoldi, L.A. Antonelli, P. Antoranz, A. Babic, et al. The major upgrade of the MAGIC telescopes, Part I: The hardware improvements and the commissioning of the system. 2014.

[4] J. Aleksic, S. Ansoldi, L.A. Antonelli, P. Antoranz, A. Babic, et al. Black hole lightning due to particle acceleration at subhorizon scales. *Science*, 346:1080–1084, 2014. doi: 10.1126/science.1256183.

[5] J. Aleksic et al. MAGIC Gamma-Ray Telescope Observation of the Perseus Cluster of Galaxies: Implications for Cosmic Rays, Dark Matter and NGC 1275. *Astrophys.J.*, 710:634–647, 2010. doi: 10.1088/0004-637X/710/1/634.

[6] J. Aleksic et al. Constraining Cosmic Rays and Magnetic Fields in the Perseus Galaxy Cluster with TeV observations by the MAGIC telescopes. *Astron.Astrophys.*, 541:A99, 2012. doi: 10.1051/0004-6361/201118502.

[7] J. Aleksic et al. The major upgrade of the MAGIC telescopes, Part II: The achieved physics performance using the Crab Nebula observations. 2014.

[8] Shin'ichiro Ando and Koji Ishiwata. Constraints on decaying dark matter from the extragalactic gamma-ray background. *JCAP*, 1505(05):024, 2015. doi: 10.1088/1475-7516/2015/05/024.

[9] JCCC Astronomy. Dark Matter and Dark Energy and the Fate of the Universe. URL `http://blogs.jccc.edu/astronomy/textbook/unit-five-galaxies-and-cosmology`. Available on line; notes assembled from Nick Strobel's Astronomy Notes.

[10] Gianfranco Bertone. Dietro le quinte dell'universo. (18), 2015, April.

[11] Xiao-Jun Bi, Peng-Fei Yin, and Qiang Yuan. Status of Dark Matter Detection. *Front.Phys.China*, 8:794–827, 2013. doi: 10.1007/s11467-013-0330-z.

[12] Marco Cirelli, Gennaro Corcella, Andi Hektor, Gert Hutsi, Mario Kadastik, et al. PPPC 4 DM ID: A Poor Particle Physicist Cookbook for Dark Matter Indirect Detection. *JCAP*, 1103:051, 2011. doi: 10.1088/1475-7516/2012/10/E01, 10.1088/1475-7516/2011/03/051.

[13] MAGIC Collaboration. Computation of upper limits (theory), 2015. URL http://wiki.magic.pic.es/index.php/Computation_of_Upper_Limit_(Theory). Available online.

[14] MAGIC Collaboration. Image cleaning (theory), 2015. URL http://wiki.magic.pic.es/index.php/Image_cleaning_(Theory). Available online.

[15] MAGIC Collaboration. Stereo reconstruction (theory), 2015. URL http://wiki.magic.pic.es/index.php/Stereo_reconstruction_(Theory). Available online.

[16] Jan Conrad. Indirect Detection of WIMP Dark Matter: a compact review. 2014.

[17] Francesco Dazzi. The MAGIC Level 1 Trigger (LT1), 2014.

[18] Doro, Michele. *Novel Reflective Elements and Indirect Dark Matter Searches for MAGIC II and Future IACTs.* Phd Thesis, University of Padova, Faculty of Sciences, Department of Physics and Astronomy "G. Galilei", 2008/2009.

[19] A.C. Fabian, Jeremy S. Sanders, G.B. Taylor, S.W. Allen, C.S. Crawford, et al. A very deep chandra observation of the perseus cluster: shocks, ripples and conduction. *Mon.Not.Roy.Astron.Soc.*, 366:417–428, 2006. doi: 10.1111/j.1365-2966.2005.09896.x.

[20] Jonathan L. Feng. Dark Matter Candidates from Particle Physics and Methods of Detection. *Ann.Rev.Astron.Astrophys.*, 48:495–545, 2010. doi: 10.1146/annurev-astro-082708-101659.

[21] V.P. Fomin, A.A. Stepanian, R.C. Lamb, D.A. Lewis, M. Punch, et al. New methods of atmospheric Cherenkov imaging for gamma-ray astronomy. 1: The False source method. *Astropart.Phys.*, 2:137–150, 1994. doi: 10.1016/0927-6505(94)90036-1.

[22] Pauline Gagnon. How do we know Dark Matter exists? URL http://www.quantumdiaries.org/2013/06/26/does-dark-matter-really-exist/. Available on line.

[23] Graciela B. Gelmini. TASI 2014 Lectures: The Hunt for Dark Matter. 2015.

[24] L. Goembel. Large geometric factor charged particle spectrometer, March 9 2004. URL http://www.google.com/patents/US6703612. US Patent 6,703,612.

[25] Kamioka-cho Higashi-Mozumi. Proton decay search, 2010. URL http://www-sk.icrr.u-tokyo.ac.jp/sk/physics/pdecay-e.html. Available online.

[26] Alejandro Ibarra, David Tran, and Christoph Weniger. Indirect Searches for Decaying Dark Matter. *Int.J.Mod.Phys.*, A28:1330040, 2013. doi: 10.1142/S0217751X13300408.

[27] Prof. Justin Read. Astrophysical probes of dark matter, 2014.

[28] Randy Russel. Solar Energy in Earth's Atmosphere. URL `http://www.windows2universe.org/earth/Atmosphere/earth_atmosph_radiation_budget.html`. Available on line.

[29] Miguel A. Sanchez-Conde, Mirco Cannoni, Fabio Zandanel, Mario E. Gomez, and Francisco Prada. Dark matter searches with Cherenkov telescopes: nearby dwarf galaxies or local galaxy clusters? *JCAP*, 1112:011, 2011. doi: 10.1088/1475-7516/2011/12/011.

[30] Schultz, Cornelia Hanna Esther. *Development of New Composite Mirrors for Imaging Cherenkov Telescopes and Observations of the Two Blazar Objects 1ES 0806+524 and 1ES 1011+496 with MAGIC*. Phd Thesis, University of Padova, Faculty of Sciences, Department of Physics and Astronomy "G. Galilei", 2012/2013.

[31] Mark Whittle. Spiral Rotation Curves. URL `https://www.astro.virginia.edu/class/ whittle/astr553/Topic05/t5_rotcurv.htm`. Available on line.